The Astrophysical Journal, 987:11 (17pp), 2025 July 1 https://doi.org/10.3847/1538-4357/add68d

A Pilot Method to Determine the High Mass End of the Stellar Initial Mass Function in Galaxies Using UVIT, Hα-MUSE Observations and Applied to NGC 628

S Amrutha[1,2] and Mousumi Das[1]
[1] Indian Institute of Astrophysics, Koramangala II Block, Bangalore 560034, India; amrutha.s@iiap.res.in
[2] Pondicherry University, R.V. Nagar, Kalapet, 605014, Puducherry, India
Received 2024 November 26; revised 2025 April 28; accepted 2025 May 4; published 2025 June 23

Abstract

We present a pilot method to estimate the high-mass initial mass function (IMF) across the arm, interarm, and spur regions in galaxies and apply it to NGC 628. We extracted star-forming complexes (SFCs) from the Hα Very Large Telescope/Multi Unit Spectroscopic Explorer and Ultraviolet Imaging Telescope (far-ultraviolet (FUV) and near-ultraviolet (NUV)) observations of NGC 628 and used Atacama Large Millimeter/submillimeter Array observations to define the molecular gas distribution. We find that the extinction-corrected Hα and FUV luminosities correlate well. Using the fact that O stars have a shorter lifetime (10^7 yr) compared to B stars (10^8 yr), we estimated the approximate number of O stars from Hα emission, and the number of B0 ($M_* > 10M_\odot$), and B1 ($10M_\odot \geqslant M_* \geqslant 3M_\odot$) stars using FUV and NUV observations. We derived the IMF index (α) for different regions using O to B0 (α_1) and B0 to B1 (α_2) stellar ratios. Our findings indicate that if we assume Hα arises only from O8-type stars, the resulting α_1 value is consistent with the canonical IMF index. It steepens when we assume O stars with masses up to 100 $M_\odot$ with mean $\alpha_1 = 3.16 \pm 0.62$. However, the α_2 does not change for large variations in the O-star population, and the mean $\alpha = 2.64 \pm 0.14$. When we include only blue SFCs (FUV − NUV $\leqslant$ 0.3), mean α_2 is 2.43 $\pm$ 0.06. The IMF variation for SFCs in arms and spurs is insignificant. We also find that α_2 correlates with different properties of the SFCs, the most prominent being the extinction-corrected UV color (FUV − NUV).

Unified Astronomy Thesaurus concepts: Star forming regions (1565); Initial mass function (796); Galaxies (573); Spiral galaxies (1560); Ultraviolet astronomy (1736); Massive stars (732)

Materials only available in the online version of record: machine-readable table

1. Introduction

Stars in galaxies are generally found in star clusters and stellar associations (J. M. Scalo 1986a). The masses of the stars formed in a cluster vary over a wide range and depend on several factors, such as the environment, metallicity, and density of the parent molecular cloud. This distribution of stellar masses formed during the star formation event in a given volume is called the initial mass function (IMF; P. Kroupa 2002). The IMF is a crucial ingredient for the stellar evolution models of star-forming galaxies (e.g., C. Leitherer et al. 1999; G. Bruzual & S. Charlot 2003; C. Maraston 2005) and is thus essential for understanding star formation as well as galaxy formation and evolution (N. Bastian et al. 2010).

Over the past few decades, many studies have tried to understand the IMF using resolved populations of stellar clusters in the solar neighborhood, within the Milky Way, and in nearby galaxies lying in the Local Group (E. E. Salpeter 1955; D. R. Weisz et al. 2015; T. M. Wainer et al. 2024). The IMF is commonly described by a power-law form with an index $\alpha = 2.35$, where $dN/dm = Am^{-\alpha}$, A is a constant, and dN/dm represents the number of stars formed in a mass range dm (E. E. Salpeter 1955). Even the canonical stellar IMF is closer to value 2.3 for stars with $M_* > 0.5M_\odot$. This IMF is observed for the field stars and nearby star-forming regions of sizes approximately equal to one parsec (T. Jeřábková et al. 2018). In general, α is observed to be shallower for low-mass stars ($M_* < 0.5M_\odot$) (P. Kroupa 2001; G. Chabrier 2003). Determining the uniformity of the IMF for all stellar populations involves combining IMF estimates for different resolved populations. However, estimating IMF in different mass ranges has its own challenges (P. Kroupa 2002).

Several studies have tried to understand the universality of the IMF (e.g., E. A. Hoversten & K. Glazebrook 2008; G. R. Meurer et al. 2009; S. Dib 2014). Recent studies have shown that the IMF is nonuniversal and depends on environmental and statistical effects (J. Pflamm-Altenburg & P. Kroupa 2008; M. R. Krumholz 2014; P. Sharda & M. R. Krumholz 2022; T. S. Tanvir et al. 2022). The denser starburst galaxies have a top-heavy IMF, i.e., a large number of massive stars, and hence an IMF that is flatter than the canonical IMF. In comparison, the less dense, low surface-brightness galaxies show a bottom-heavy IMF (i.e., steeper than the canonical IMF; J. Scalo 1990; E. A. Hoversten & K. Glazebrook 2008; G. R. Meurer et al. 2009; C. Weidner et al. 2011). Even within galaxies, there are regions with low stellar surface mass densities, such as the outer disks of extended UV (XUV) galaxies or the interarm regions of spiral galaxies where the IMF can be different compared to that of the spiral arms (D. A. Thilker et al. 2007; P. Kroupa et al. 2024).

In this study, we focus on the high-mass end of the IMF. Massive stars significantly impact the chemical enrichment of the interstellar medium due to their strong stellar winds and feedback process (D. Chappell & J. Scalo 2001; T. Freyer et al. 2003). Hence, it is essential to understand the upper or high-mass end of the IMF, even though the low-mass stars contribute more to cluster masses, as well as the overall mass of a galaxy. Young massive stars emit most of their energy at far-ultraviolet (FUV) wavelengths and have a short main sequence. However, it is difficult to distinguish between the two main types of massive stars (O and B, $M_* > 20M_\odot$) based on just magnitude alone (P. Kroupa 2002). Even with *UV* colors, it is challenging to distinguish massive B stars from O stars (J. Koda et al. 2012). Massive O-type stars give out FUV, near-ultraviolet (NUV), and Hα emission. The Hα emission from O and massive B stars is a well-known tracer of star formation in galaxies (R. C. J. Kennicutt et al. 2009; J. C. Lee et al. 2009). But Hα can trace star formation for only 10 Myr, since O star lifetimes vary from 1 to 10 Myr. However, UV traces O, B, and even some red and cold stars, which makes them trace star formation for around 200 Myr (D. A. Thilker et al. 2005). Therefore, recent studies have used both UV and Hα measurements to understand the universality of the high-mass end of the IMF by considering the relative strength of their emission in external galaxies (J. C. Lee et al. 2009; G. R. Meurer et al. 2009; J. Koda et al. 2012).

Previous studies have used Galaxy Evolution Explorer (GALEX) data to show that there is a correlation between the star formation rate (SFR) and the Hα to UV flux ratios in galaxies (J. C. Lee et al. 2009; G. R. Meurer et al. 2009; D. A. Hunter et al. 2010). They also show that the galaxies with low SFRs have a deficit of O stars, and hence have bottom-heavy IMF due to stochastic sampling. A. Boselli et al. (2009) used Hα to UV ratios to show that the high-mass end of late-type normal galaxies follows the standard IMF. D. Calzetti et al. (2010) showed that a universal IMF exists by comparing the Hα flux with the cluster mass. Some studies have investigated the high end of the IMF in the outskirts of XUV galaxies and find that the bottom-heavy IMF dominates (S. M. Gogarten et al. 2009; S. M. Bruzzese et al. 2019). In contrast, some studies show that it follows the standard IMF (J. Koda et al. 2012). A few studies analyzed the IMF in XUV disks by assuming that the Hα to UV flux ratios are approximately equal to the ratios between the lifetime of the stars that can produce Hα to those that produce UV emission (i.e., mainly O and B types stars; D. Zaritsky & D. Christlein 2007). S. M. Bruzzese et al. (2019) used Hubble Space Telescope (HST) measurements and compared them with the simulations to obtain the high-mass end of the IMF.

This paper presents a new method to determine the slope α of the high-mass end of the IMF using observations of individual star-forming complexes (SFCs). We leverage the high sensitivity and spatial resolution of the Ultraviolet Imaging Telescope (UVIT) and Multi Unit Spectroscopic Explorer (MUSE) to extract the SFCs of a nearby galaxy to determine the ratio of O and B stars to derive α. We investigate whether α varies with regions, i.e., spiral arms, spurs, and interarm regions, since the mechanisms leading to star formation in these regions are different. Spiral arms are global disk instabilities, whereas star formation in the spurs or feathers is due to local gas instabilities, where diffuse gas is transformed into dense gas when it flows into the spiral arm. The inflow shocks the gas near the arm and causes star formation in these spur regions (W.-T. Kim & E. C. Ostriker 2002; R. Shetty & E. C. Ostriker 2006). The interarm regions have isolated SFCs, and the star-forming mechanism may be more local. Many studies have attempted to understand star formation in both the spiral arm and interarm regions, but our analysis focuses on the IMF (S. Stedman & J. H. Knapen 2001; K. Foyle et al. 2010; D. J. Eden et al. 2013). Studying the IMF over different regions of a galaxy will also help us understand the universality of the IMF within a galaxy.

To test our new method, we applied it to the nearby face-on galaxy NGC 628. In Section 2, we briefly introduce the NGC 628 and discuss the data. Section 3 discusses the methods used to extract the complexes, correct for the extinction, and the characterization of the SFCs. In Sections 4 and 5, we present and discuss the results of our IMF study over different regions and how it depends on the properties of the SFCs.

2. NGC 628 and Observations

NGC 628, also known as M74 or the Phantom Galaxy, is a grand design spiral galaxy of Hubble type SA(s)c (G. de Vaucouleurs et al. 1991), and is at a distance of 9.84 Mpc (G. S. Anand et al. 2020). This massive galaxy ($\log(M_*/M_\odot) = 10.34$; A. K. Leroy et al. 2019) is nearly face-on ($i = 8\overset{\circ}{.}9$; P. Lang et al. 2020) with a position angle of $20\overset{\circ}{.}7$ (P. Lang et al. 2020). Hence, it is the perfect target for studying star formation properties in different regions of a galaxy. The star formation in NGC 628 is well studied (K. Kreckel et al. 2016, 2018; M. Lomaeva et al. 2022) and the SFCs on kpc scales have also been characterized (J. Yadav et al. 2021; K. Ujjwal et al. 2022). We used archival, deep UV imaging observations obtained using the UVIT on board the AstroSat telescope (A. Kumar et al. 2012) to understand IMF. The UVIT is a twin telescope with coaligned Ritchey–Chrétien (RC) optics. One of the telescopes is FUV (1300–1800Å) and the other has NUV (2000–3000Å) and visible (VIS) bands. The instrument has a field of view of $0\overset{\circ}{.}5$ and can observe simultaneously in all three bands. The FUV and NUV have a resolution around $1\overset{''}{.}2$–$1\overset{''}{.}5$ sampled at $0\overset{''}{.}417$ per pixel (S. N. Tandon et al. 2020). This resolution is three to four times better than GALEX (D. C. Martin et al. 2005).

We downloaded Level 1 data from the Indian Space Science Data Centre (ISSDC) website.[3] The UVIT observed NGC 628 in multiple filters, but we used the CaF2 F148W FUV image with an exposure time of 1810 s and a bandwidth of 500 Å, and the NUVB4 N263M image, which has an exposure time of 2086 s and a bandwidth of 275 Å, for our analysis. We also used two close filters, F172M (bandwidth and exposure time are 125Å and 5881 s, respectively) and N219M (bandwidth and exposure time are 270 Å and 1365 s, respectively), to correct internal extinction using the Beta slope as described in Section 3.2.

We obtained archival MUSE (E. Emsellem et al. 2022) Hα and Hβ maps, archival Atacama Large Millimeter/submillimeter Array (ALMA; A. K. Leroy et al. 2021a, 2021b) CO($J = 2$–1) moment 0 map, and also the James Webb Space Telescope (JWST; J. C. Lee et al. 2023) F2100W map, from the PHANGS Treasury Program.[4] The Very Large Telescope's (VLT's) MUSE observations provide a field of view of one arcmin × one arcmin, with a high spatial resolution of $0\overset{''}{.}6$ PSF FWHM sampled at $0\overset{''}{.}2$ per pixel. Whereas ALMA has a resolution around 1″ sampled at $0\overset{''}{.}2$ per pixel. The JWST F2100W map has a central wavelength approximately equal to 21 μm and a resolution of $0\overset{''}{.}67$ sampled at $0\overset{''}{.}11$ per pixel.

3. Data Analysis

3.1. Source Extraction and Classification

We reduced the raw UVIT data using the CCDLAB graphical user interface (J. E. Postma & D. Leahy 2017). This interface corrects field distortions, flat-fielding, and drift.

[3] https://astrobrowse.issdc.gov.in/astro_archive/archive/Home.jsp
[4] https://sites.google.com/view/phangs/home

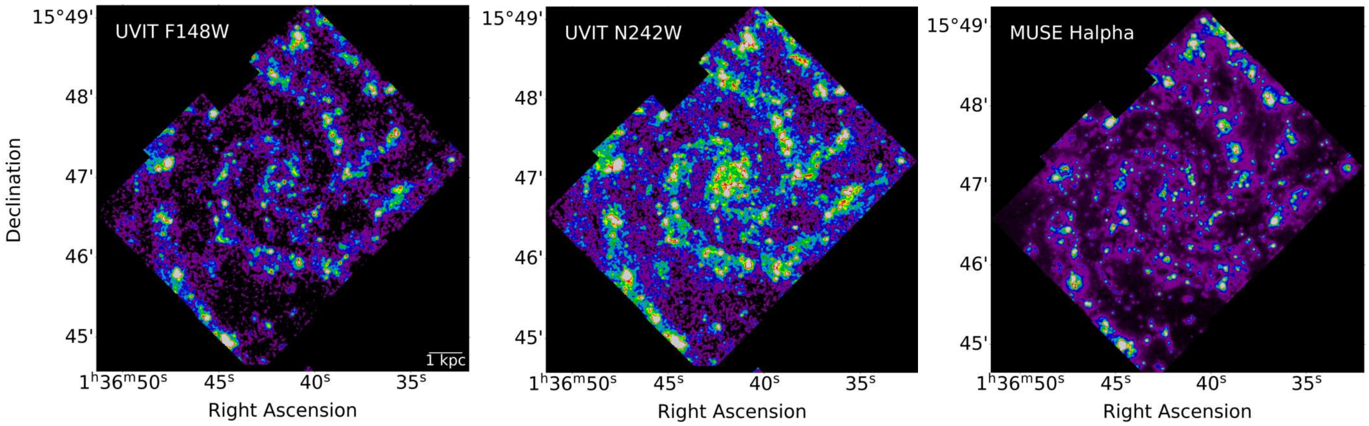

Figure 1. UVIT FUV, NUV, and MUSE Hα images of galaxy NGC 628 tracing recent star formation.

Later, it combines the orbit-wise UVIT images to create a final deep image. We then did the astrometry using the same interface. We did background subtraction of these images using IRAF, as mentioned in S. Amrutha et al. (2024). Using around 5–6 stars in the FUV and NUV image fields, we found that the mean PSF of the field stars is around 1.″2. Hence, this is assumed to be the resolution of the UV images. This resolution corresponds to a physical scale of 57 pc at the distance of NGC 628, which is moderately high resolution and cannot resolve star clusters because clusters have radii of a few of parsec (J. E. Ryon et al. 2015). However, we can resolve OB associations and SFCs with this resolution because they correspond to a scale of a few hundred parsec (D. M. Elmegreen et al. 2014; S. Amrutha et al. 2024).

Since we are interested in comparing the Hα and UV emission, we made cutouts of the UVIT FUV and NUV images that match the size of the MUSE Hα map. The cutout images of the FUV, NUV, and Hα maps are shown in Figure 1. We convolved the Hα map to the UV resolution of 1.″2. We extracted SFCs in all three images using the command line program Source Extractor (SExtractor; E. Bertin & S. Arnouts 1996). We set the detection threshold to five times the estimated global background noise for confident detection. Then, we masked the foreground sources (with high parallax and high proper motion) by comparing the extracted SFCs with the bright sources in the Gaia catalog using TOPCAT (M. B. Taylor 2005). We also convolved the Hβ and JWST map to the UVIT resolution.

We determined the total counts from the extracted SFCs using the Photutils module (Astropy Collaboration et al. 2018). The UV fluxes were derived using the conversion relation $\text{Flux} = \text{UC} \times \text{CPS}_{\text{corr}}$, as mentioned in S. N. Tandon et al. (2017), where UC is unit conversion factor in $\text{erg s}^{-1}\,\text{cm}^{-2}\,\text{A}^{-1}$ and CPS_{corr} is the counts per second corrected for Milky Way extinction (E. F. Schlafly & D. P. Finkbeiner 2011) for the FUV and NUV filters (A. Bayo et al. 2008). We determined the UV and Hα luminosities in erg s^{-1} units using the distance of the galaxy and the bandwidth of the UV filters.

We matched the UV and Hα images and found the SFCs that are present in all three filters. We also determined the SFCs that are detected only in the FUV and Hα filters, the SFCs detected only in the NUV and Hα filters, and finally, the SFCs detected in only the FUV and NUV filters. We also found the SFCs that are visible only in FUV, only in NUV, and also only in Hα. This classification was necessary because we needed emissions from all three bands to estimate the IMF value.

We noted the SExtractor parameters of the SFCs with larger areas present in at least two filters. We also classified them as arm, interarm, and spur SFCs based on location. This classification helps us understand the universality of the IMF within the galaxy. Hence, we first classified the SFCs as arms and interarm sources based on their location in the NUV image (see Figure 2(a)). Then, we again checked which SFCs lie in and around the spur regions of the ALMA observations (Figure 2(b)).

3.2. Internal Extinction Correction

An accurate extinction correction of observed Hα and UV luminosities is crucial for IMF analysis. Since there are different methods to correct the galaxy's internal extinction, we corrected SFC luminosities for internal extinction using the Balmer decrement, Beta slope, and JWST 21 μm methods to see which method gives a better correlation for Hα and UV luminosities. We used Hα and Hβ maps of MUSE to find the Balmer decrement, which is one of the most successful techniques for determining dust extinction. It uses the ratio of two nebular Balmer emission lines such as Hα and Hβ at low redshifts (R. C. J. Kennicutt 1992; J. R. C. Moustakas et al. 2006; T. Garn & P. N. Best 2010). The intrinsic ratio of the two lines remains roughly constant for typical gas conditions in star-forming galaxies and $\left(\frac{\text{H}\alpha}{\text{H}\beta}\right)_{\text{int}} = 2.86$, at the temperature 10^4 K and an electron density $n_e = 10^2\,\text{cm}^{-3}$ for Case B recombination (D. E. Osterbrock 1989). Hence, the corresponding color excess $E(B-V)$ is given by,

$$E(B - V) = 1.97 \log_{10}\left[\frac{\left(\frac{\text{H}\alpha}{\text{H}\beta}\right)_{\text{obs}}}{2.86}\right], \tag{1}$$

and using the D. Calzetti et al. (2000) reddening curve, we find the Hα extinction to be, $A_{\text{H}\alpha} = (3.33 \pm 0.80) \times E(B-V)$.

For the SFCs with FUV and Hα emission, we found FUV extinction using the relation, $A_{\text{FUV}} = 3.6 A_{\text{H}\alpha}$, assuming that the FUV emission arises mainly from the young stellar population as mentioned in A. K. Leroy et al. (2008) and we corrected for the extinction in NUV band using relation $A_{\text{NUV}} = 0.8 A_{\text{FUV}}$ (D. Calzetti et al. 2000). The extinction-

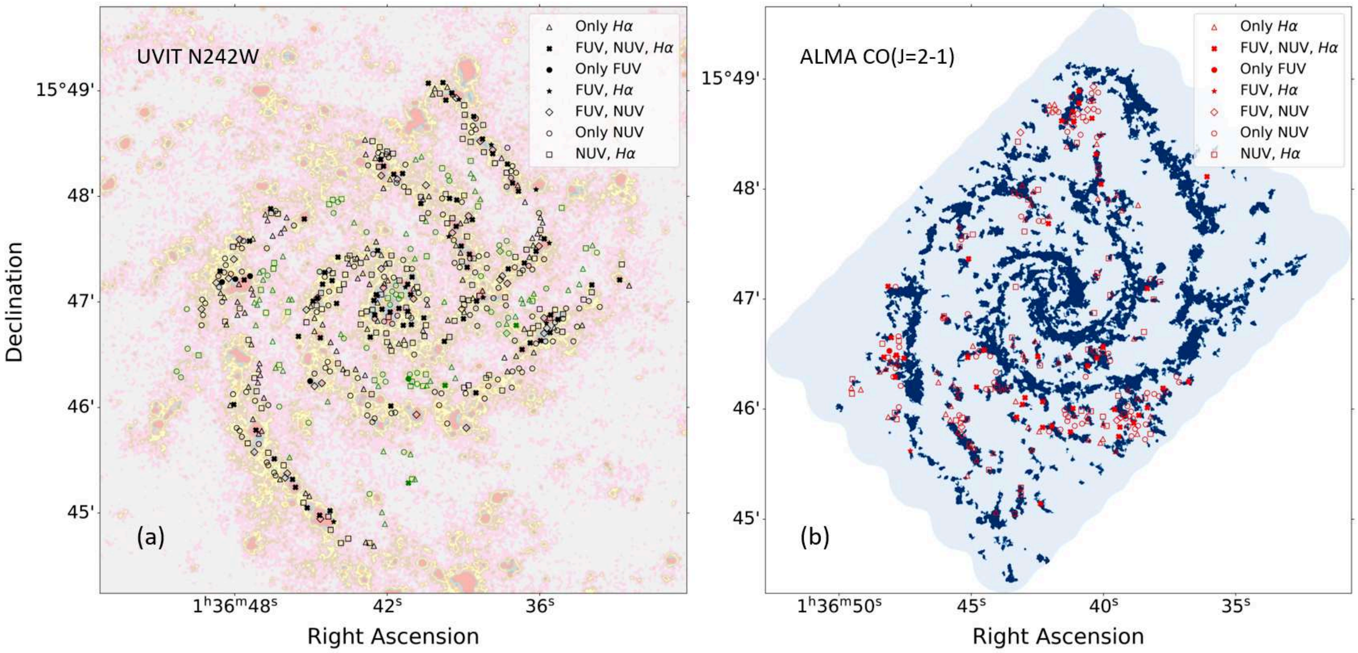

Figure 2. The above images show the classification of SFCs based on their region(different colors) and their emission in different filters (different markers). Image (a): The locations arm (black markers) and interarm (green markers) SFCs overplotted on UVIT NUV image. Image (b): The locations of spurs(red markers) SFCs overplotted on the ALMA CO($J = 2$–1) image.

corrected Hα and UV luminosity is given by

$$L(\lambda)_{\rm corr} = 10^{0.4A_\lambda} L(\lambda)_{\rm obs}, \tag{2}$$

where $L(\lambda)_{\rm obs}$ is observed luminosity at the wavelength λ. The correlation of extinction-corrected Hα and UV luminosity for SFCs using the Balmer decrement method is shown in Figures 3(c) and (f).

The Beta slope method can be used for the SFCs with FUV and NUV emission to correct the internal extinction (D. Calzetti et al. 1994). The extinction curve in the *UV* band (1300–2600 Å) can be fitted by a power law with the slope β ($f_\lambda \propto \lambda^\beta$). The UV spectral slope is filter-dependent, and we can get a better estimate for β when we consider the two close filters. Hence, β for *UVIT* filters $m_{\rm F172M}$ and $m_{\rm N219M}$ is given by,

$$\beta = \frac{m_{\rm F172M} - m_{\rm N219M}}{-2.5\log(\frac{\lambda_{\rm F172M}}{\lambda_{\rm N219M}})} - 2, \tag{3}$$

where $m_{\rm F172M}$ and $m_{\rm N219M}$ are the Galactic extinction-corrected magnitudes of SFCs in the F172M and N219M filters with $\lambda_{\rm F172M}$ and $\lambda_{\rm N219M}$ as their central wavelengths, respectively. Then, we used filters F148W and N263M and found the SFC's extinction $A_\lambda = (0.44 \pm 0.03)E(B-V)k(\lambda)$ as given by D. Calzetti et al. (2000). The color excess $E(B-V)$ is then found using $\beta = -2.616 + 4.594E(B-V)$ as given by N. A. Reddy et al. (2018) and $k(\lambda)$ as given in D. Calzetti et al. (2000) for filters F148W and N263M, and for SFCs with Hα emission. We again calculated extinction-corrected Hα and UV luminosities for this method using Equation (2).

Apart from the two methods mentioned above, we use 24 μm to measure the embedded Hα and UV luminosities, as mid-IR peaks around 24 μm and traces the hot dust component that is due to the young stellar population. In addition, F. Belfiore et al. (2023) showed that the F2100W filter of JWST is better for extinction correction than any of the other mid-IR bands in JWST. Hence, here we corrected for extinction using a convolved JWST 21 μm map. We used the extinction correction relation for Hα as given in R. C. J. Kennicutt et al. (2009) and for FUV and NUV as in C.-N. Hao et al. (2011). The relation for finding the extinction-corrected luminosity is $L(\lambda)_{\rm corr} = L(\lambda)_{\rm obs} + cL(24\,\mu{\rm m})$. Here, $L(\lambda)_{\rm corr}$ and $L(\lambda)_{\rm obs}$ are the corrected luminosity and observed luminosity in erg s^{-1}, respectively. The parameter c is 3.89, 2.26, and 0.0024 when we correct the FUV, NUV, and Hα luminosities, respectively. $L(24\,\mu{\rm m})$ is the Spitzer MIPS 24 μm luminosity in erg s^{-1}. Since we are using the JWST 21 μm map, we took the ratio of JWST 21 μm and MIPS 24 μm luminosity for some of the SFCs on both maps. We find that the ratio is approximately equal to 4.54. We multiplied this value with $L(21\,\mu{\rm m})$ to obtain the $L(24\,\mu{\rm m})$.

We plotted the extinction-corrected Hα and UV luminosity correlations for all three methods in Figures 3(b) and (e). The extinction-corrected luminosities strongly correlate for SFCs corrected with the Balmer decrement and JWST methods. However, we see a clear difference between the three methods in Figure 3(e), which reveals that each method uniquely compensates for extinction at varying depths. Hence, it is necessary to use a single method to correct extinction. The SFC luminosities corrected with the Beta slope method show more scatter ($\sigma_{\rm FUV} = 0.38$ and $\sigma_{\rm NUV} = 0.37$), making it less preferable. Although the JWST 21 μm method showed a tight Hα and UV luminosity correlation ($\sigma_{\rm FUV} = 0.17$ and $\sigma_{\rm NUV} = 0.17$), due to its limited field of view, very few SFCs had 21 μm emission. Hence, we mainly used the Balmer decrement method ($\sigma_{\rm FUV} = 0.21$ and $\sigma_{\rm NUV} = 0.25$) for the extinction correction for SFCs with Hα luminosity; the SFCs without Hα luminosity were not used for further analysis wherever Hα and UV luminosities are involved. However, we have shown the extinction-corrected Hα and UV luminosity correlation for the Balmer decrement method and also the SFR correlations for the Balmer decrement and JWST methods in Section 4.2.

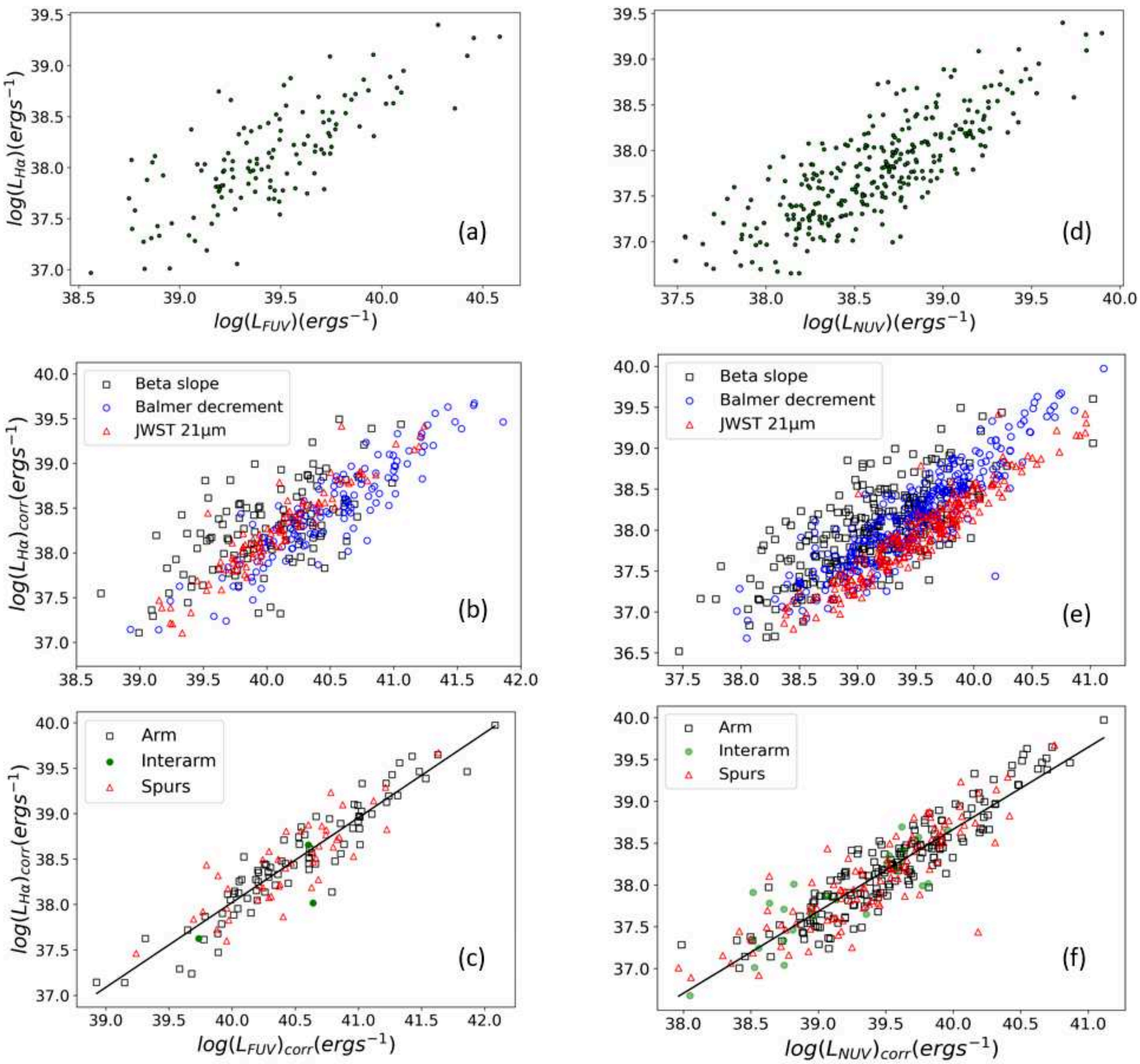

Figure 3. Figures on the left ((a), (b), and (c)) and on the right ((d), (e), and (f)) illustrate the correlation of Hα luminosity with FUV and NUV luminosities, respectively, for the SFCs. Figures (a) and (d): Luminosities presented without any correction for internal dust attenuation. Figures (b) and (e): Luminosities are corrected for internal dust attenuation using different methods indicated with different symbols and colors. Figures (c) and (f): Luminosities corrected for internal dust attenuation using the Balmer decrement method for the SFCs with Hα emission, and the scaling relation is used to find the FUV extinction coefficient. The fitted relations related to these plots are given in Section 4.2.

3.3. Characterization of the SFCs

We calculated the FUV SFR for the SFCs using S. Salim et al. (2007). The FUV SFR in $M_{\odot}\mathrm{yr}^{-1}$ is given by $\mathrm{SFR_{FUV}} = 0.68 \times 10^{-28} \times L(\mathrm{FUV})_{\mathrm{corr}}$. Similarly, we calculated the Hα SFR using D. Calzetti et al. (2007) given by $\mathrm{SFR_{H\alpha}} = 5.3 \times 10^{-42} \times L(\mathrm{H}\alpha)_{\mathrm{corr}}$. Here, $L(\mathrm{FUV})_{\mathrm{corr}}$ and $L(\mathrm{H}\alpha)_{\mathrm{corr}}$ are the extinction-corrected luminosities in erg s^{-1}. As mentioned in Section 3.2, we only derived both FUV and Hα SFRs for SFCs with associated Hα luminosity. We calculated the SFR density Σ (SFR) by dividing the SFRs by respective areas.

We also derived the corresponding stellar masses of the SFCs using starburst99 and a simple stellar population model (C. Leitherer et al. 1999). Starburst99 is a set of spectrophotometric model predictions that can be used to find the properties of star-forming galaxies. We ran starburst99 assuming Padova tracks with asymptotic giant branch stars and standard Salpeter IMF (E. E. Salpeter 1955) with the lower cutoff mass set to $m_l = 0.1 M_{\odot}$ and the upper cutoff mass to be $m_u = 100 M_{\odot}$. We adopted a solar metallicity ($Z = 0.02$; C. Leitherer et al. 1999), which is closer to the value mentioned in D. Calzetti et al. (2015). We evolved the model from 1 to 200 Myr, since UV can trace up to 200 Myr. We plotted the observed extinction-corrected UV color and FUV magnitudes of the SFCs on the theoretically predicted values from Starburst99. We then interpolated the values for each SFC to find the mass.

We estimated the molecular hydrogen mass using the ALMA CO($J = 2$–1) map. We converted the CO flux to H_2 mass using

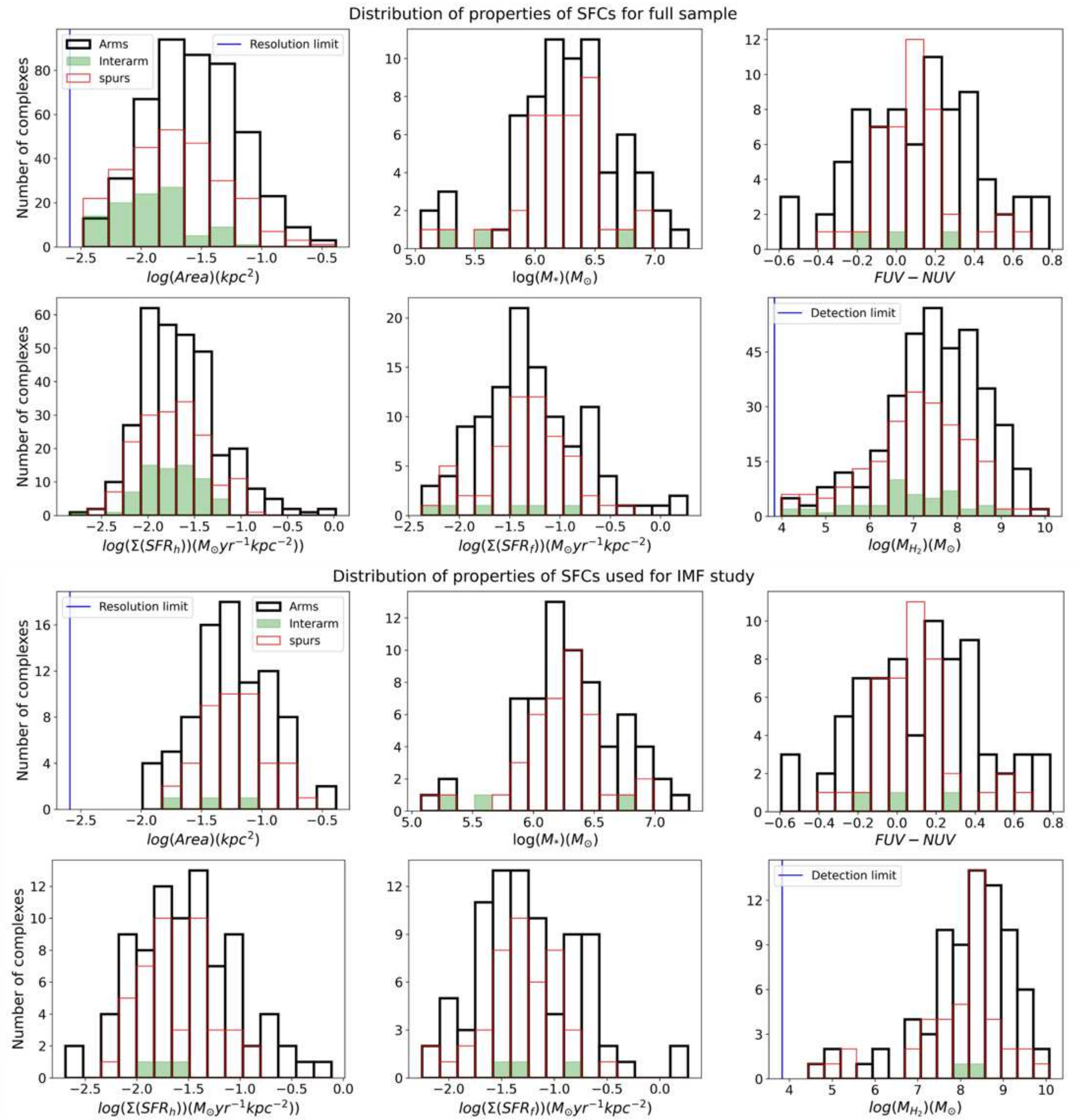

Figure 4. The distribution of star formation properties across different regions (arms, spurs, and interarm) for all available SFCs (first two rows) and specifically for the SFCs used in the IMF analysis.

the conversion factor $\alpha_{CO} = 4.35 M_\odot \mathrm{pc}^{-2}(\mathrm{K\ km\ s^{-1}})^{-1}$ and $R_{21} = 0.62$ (K. M. Sandstrom et al. 2013; K. Kreckel et al. 2018).

We plotted the distribution of different properties of SFCs, such as the area (from SExtractor), molecular hydrogen mass (M_{H_2}), extinction-corrected FUV and NUV color (FUV − NUV), stellar mass (M_*), and Σ(SFR), for both Hα and FUV emission for all the possible SFCs (for area and M_{H_2} distribution, we included even the SFCs which did not have emission in all three bands) and also for the SFCs used for IMF analysis, as shown in Figure 4. We also observed that the median estimated values of properties such as (M_*) and area of SFCs are more than what we see in resolved studies of stellar clusters in NGC 628 with HST in the Legacy ExtraGalactic UV Survey (A. Adamo et al. 2017) because SFCs contain multiple individual star-forming clusters and smaller OB associations.

3.4. The Number of High-mass Stars and their Ratios in the SFCs

This section describes how we estimated the approximate number of O and B stars in the SFCs. It depends crucially on the difference in timescales over which Hα and UV emission trace star formation. The Hα and FUV emission arise from O stars and massive B stars. But since Hα comes from recombination in the ionization region around massive stars, it lasts for a few Myr. Even if we consider that there is a contribution from B stars in the Hα emission, we may not get the total count of massive B stars. Hence, for this study, we assume that the $H\alpha$ emission arises mainly from O stars. The FUV emission arises from O ($M > 21 M_{\odot}$), and also massive B0 stars ($M > 10 M_{\odot}$). We also see that with 5σ photometric limit of FUV and NUV filters, we can only detect individual stars after O7 stars. But, since low-mass stars are more in number, and studies have shown that NUV can significantly detect emission from even low-mass B stars (M. Das et al. 2021), we assume that the NUV emission arises from O, B0, and B1 stars ($M \leqslant 10 M_{\odot}$). All of this information can be used to estimate the number of O, B0, and B1 stars as described below.

Given that we do not know what kind of O stars produce the Hα emission from the SFCs, we randomly populate O stars in the SFCs by assigning a fraction of the Hα luminosity for each type of O star we are considering. Here, we present the three cases. First, we consider that Hα arises from only O8V-type stars (31 $M_{\odot}$). Second, we consider that Hα comes from only O7V, O8V, and O9V stars. We included these types of O stars because previous studies show that the median Hα luminosity of the SFCs in NGC 628 corresponds to the luminosity of a single O8V star (K. Kreckel et al. 2016). Finally, apart from these two combinations, we tried a third case in which we populate the SFCs with a combination of O9V (23 $M_{\odot}$) to O3V stars (88 $M_{\odot}$). In this way, we include different combinations of O-type stars to estimate how the IMF varies. We used the Hα Lyman photon flux $Q_{\rm H}$ for each stellar type from A. Sternberg et al. (2003). We consider Case B recombination with electron temperature 10^4 K (G. Gavazzi et al. 2002). The Hα luminosity in erg s^{-1} is given by $1.37 \times 10^{-12} Q_{\rm H}[{\rm s}^{-1}]$. The F. Castelli & R. L. Kurucz (2004) model was used to find the FUV and NUV luminosities for these stars. We chose the closest parameters, such as effective temperature ($T_{\rm eff}$), surface gravity (g), and radius (R), from the grid of all types of O, B0, and B1 star models from A. Sternberg et al. (2003) and C. Leitherer et al. (2010), where the B1 stars parameter are from the second paper and the rest from the first paper. The parameters ($T_{\rm eff}$, log(g), R), along with the UV luminosities for the solar metallicity, are given in Table 1.

Initially, the algorithm carried out 10,000 iterations for each SFC, drawing a random Hα luminosity probability for each type of O star from a uniform distribution between 0 and 1. For the third case, we ensured that there should be at least one of each type of O star in an SFC. Then, the total number of O stars present in an SFC for each of the three cases is,

$$N(\mathrm{O}) = \sum_{n=3}^{9} \frac{P(\mathrm{O}n) \times L_{\mathrm{H}\alpha}}{L_{\mathrm{H}\alpha}(\mathrm{O}n)}, \quad (4)$$

where $L_{\mathrm{H}\alpha}$ is the Hα luminosity of an SFC and $L_{\mathrm{H}\alpha}$(On) is the Hα luminosity of single On star, where n is the class (e.g., $n = 3$, O3 type star). P(On) is the randomly generated probability for an On-type star, such that $\sum_{n=3}^{9} P(\mathrm{O}n) = 1$. For the second case, we generated the P(On) only for the combination of O7, O8, and O9 stars. For the first case, the P (O8) = 1. The number of B0 stars in the SFC derived from the FUV luminosity is,

Table 1
FUV and NUV Luminosities of Massive Stars

OV star Type	$T_{\rm eff}$ (kK)	log(g) (cm s^{-2})	$L_{\rm FUV}$ (erg s^{-1})	$L_{\rm NUV}$ (erg s^{-1})
O3	50	5	4.6×10^{38}	3.96×10^{37}
O4	47.5	5	3.5×10^{38}	3.1×10^{37}
O5	45	4.5	2.75×10^{38}	2.48×10^{37}
O6	42.5	4.5	2.18×10^{38}	2×10^{37}
O7	40	4.5	1.67×10^{38}	1.65×10^{37}
O8	38.5	4.5	1.27×10^{38}	1.29×10^{37}
O9	35.5	4	9.13×10^{37}	1.01×10^{37}
B0	33.3	4	7.26×10^{37}	8.17×10^{36}
B1	25	3.9	6.2×10^{36}	8.02×10^{35}

Note. $T_{\rm eff}$ and log(g) are the effective temperature and surface gravity parameters given to the F. Castelli & R. L. Kurucz (2004) model to get FUV luminosities ($L_{\rm FUV}$) and NUV luminosities ($L_{\rm NUV}$). We took distance 9.84 Mpc, and the star's radius as mentioned in A. Sternberg et al. (2003).

$$N(\mathrm{B0}) = \frac{L_{\rm FUV} - \sum_{n=3}^{9}(N(\mathrm{O}n) \times L_{\rm FUV}(\mathrm{O}n))}{L_{\rm FUV}(\mathrm{B0})}, \quad (5)$$

where $L_{\rm FUV}$ and $L_{\rm FUV}$(On) are the FUV luminosities of an SFC and a single On-type star, respectively. The $L_{\rm FUV}(B0)$ is the FUV luminosity of the B0 star, and N(On) is the number of On-type stars. The total number of O stars is $N(\mathrm{O}) = \sum_{n=3}^{9} N(\mathrm{O}n)$. The number of B1 stars (N(B1)) in an SFC will then be

$$N(\mathrm{B1}) = \frac{L_{\rm NUV} - (N(\mathrm{B0}) \times L_{\rm NUV}(\mathrm{B0}))}{L_{\rm NUV}(\mathrm{B1})} - \frac{\sum_{n=3}^{9}(N(\mathrm{O}n) \times L_{\rm NUV}(\mathrm{O}n))}{L_{\rm NUV}(\mathrm{B1})}, \quad (6)$$

where $L_{\rm NUV}$ and $L_{\rm NUV}$(On) are the NUV luminosity of an SFC and single On stars, respectively. In addition, $L_{\rm NUV}$(B0) and $L_{\rm NUV}$(B1) are the NUV luminosities of the B0 and B1 stars, respectively.

We then took the ratio of N(O) to N(B0) ($\frac{N(\mathrm{O})}{N(\mathrm{B0})}$) and the ratio of N(B0) to N(B1) ($\frac{N(\mathrm{B0})}{N(\mathrm{B1})}$) to obtain the IMF indices α_1 and α_2, respectively. We assume that the IMF can be represented as a distribution function in linear mass units as,

$$\frac{dN}{dm} = A m^{-\alpha}, \quad (7)$$

where α is the power-law index of the IMF. The number of stars N in the mass range m_u to m_l is

$$N = A \int_{m_l}^{m_u} m^{-\alpha} dm, \quad (8)$$

and $\frac{N(\mathrm{O})}{N(\mathrm{B0})}$ is given by,

$$\frac{N(\mathrm{O})}{N(\mathrm{B0})} = \frac{m_u(\mathrm{O})^{1-\alpha_1} - m_l(\mathrm{O})^{1-\alpha_1}}{m_u(\mathrm{B0})^{1-\alpha_1} - m_l(\mathrm{B0})^{1-\alpha_1}}, \quad (9)$$

where m_u(O) and m_u(B0) are the upper mass limit for O and B0 stars. Similarly, the lower mass limits for O and B0 stars are m_l(O), m_l(B0). m_u and m_l for the SFCs that are fully populated with O9 to O3 type stars is 21 $M_\odot$ to 100 $M_\odot$, respectively. And for B0 stars, it is 21 $M_\odot$ and 10 $M_\odot$. When we took O7, O8, and O9 stars, the m_u and m_l is 38 $M_\odot$ and 21 $M_\odot$. When considering only the O8 star, the limits are 31 $M_\odot$ and 21 $M_\odot$. All these values are adopted from A. Sternberg et al. (2003).

We also found $\frac{N(\mathrm{B0})}{N(\mathrm{B1})}$ along with the IMF index α_2

$$\frac{N(\mathrm{B0})}{N(\mathrm{B1})} = \frac{m_u(\mathrm{B0})^{1-\alpha_2} - m_l(\mathrm{B0})^{1-\alpha_2}}{m_u(\mathrm{B1})^{1-\alpha_2} - m_l(\mathrm{B1})^{1-\alpha_2}}. \tag{10}$$

The m_u and m_l for B1 stars is 10 $M_\odot$ and 3 $M_\odot$, respectively. Using the IMF index for all the SFCs, we obtained the distribution of $\frac{N(\mathrm{O})}{N(\mathrm{B0})}$ and $\frac{N(\mathrm{B0})}{N(\mathrm{B1})}$.

4. Results

4.1. Distribution of SFCs in NGC 628 in Hα, FUV, and NUV Emission.

Although NGC 628 has been observed over the whole spectrum, we focus on the bands that trace star formation in this study, i.e., FUV, NUV, and Hα. We can interpret the star formation distribution and its propagation by studying the emission at these wavelengths as they trace different timescales. Here, these emissions are characterized as SFCs, which we detected separately from each band. But the number of SFCs detected in each band depends on the threshold we have taken in SExtractor. Although taking a 5σ threshold for all bands gives us a confident bright source detection, the different sensitivities of each band may affect the number of SFCs detected, and sometimes even the area of the SFCs. However, taking SFCs that are detected in all three bands and taking the same area for all SFCs (the largest area of SFCs of the three bands) for IMF estimation makes us confident of our analysis.

The 3σ flux sensitivity of MUSE Hα is around $4–7 \times 10^{37}\mathrm{erg\,s^{-1}\,kpc^{-2}}$ (E. Emsellem et al. 2022). With a 5σ threshold, we could detect around 560 SFCs in this band. The Hα emission is more prominent in the arm and interarm regions. More than 200 SFCs are detected in the Hα map but have no associated UV emission. Some of the Hα emission could be associated with diffuse ionized gas (DIG), as indicated in previous studies (K. Kreckel et al. 2016).

The 5σ photometric limit of the UVIT F148W filter is 22.78. The FUV SFCs detected are the least numerous (around 190 SFCs) compared to the other two bands with a 5σ threshold. As mentioned above, one of the reasons could be the difference in sensitivity, which might have made us lose some faint SFCs. We see that more than 96% of the FUV SFCs are associated with SFCs in the other two bands, where only six SFCs are associated with FUV in the interarm region (out of 100 interarm SFCs). The reasons for the other 4% of FUV SFCs not having associated emissions in other bands could be due to the way SFCs are detected, such that associated SFCs could have a center that is a bit farther than the FUV SFCs. Besides this, the shock-excited accretion disk around extremely eruptive young stars emits mainly in FUV and might lack in the other two bands (A. S. Carvalho et al. 2024). Additionally, the enhancement in Hα emission from the interarm regions indicates that there could be young SFCs embedded in dust, which obscures the FUV emission. The FUV bright SFCs are also associated with the spurs along the spiral arms, which are prominent in the ALMA images.

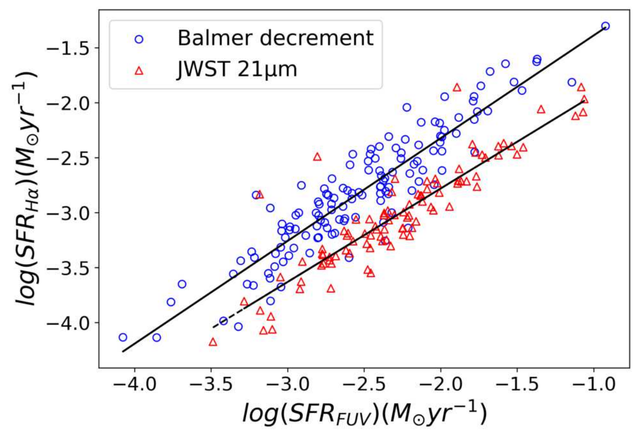

Figure 5. Observed Hα and FUV SFR correlation for SFCs corrected for extinction with the Balmer decrement and JWST 21 μm method. The linear fit for the Balmer decrement and JWST 21 μm method are given as Equations (13) and (14), respectively.

The NUV image has brighter SFCs and a smooth diffuse emission over the entire field. The galaxy center is especially bright in NUV, which we do not see in the other two bands. More NUV emission indicates that the galaxy's center has older and cooler stellar populations, and fewer massive O and B stars. The 5σ photometric limit of the UVIT N263M filter is 23.36. Of the 650 SFCs with NUV emission, more than 200 SFCs emit only NUV emission. These could be associated with evolved SFCs. The other SFCs are associated with either FUV or Hα emission, or both.

4.2. UV and Hα Luminosity Correlation

Any IMF study involving UV and Hα luminosities is susceptible to extinction correction (A. Boselli et al. 2009). Hence, choosing a method for the extinction correction is critical. When we compared the correlation of extinction-corrected luminosities using different methods, we found more scatter for luminosities corrected for extinction using the Beta slope method, as seen in Figures 3(b) and (e). Previous studies such as J. C. Lee et al. (2009) and C.-N. Hao et al. (2011) have shown that extinction-corrected UV and Hα luminosities have a strong correlation. Hence, we obtained the least-square fit for UV (FUV and NUV) and Hα luminosities, which is corrected for extinction using the Balmer decrement method. This correlation is shown in Figures 3(c) and (f) for FUV and NUV, respectively. The equations we get by fitting a regression are

$$\log(L(\mathrm{FUV})) = (0.933 \pm 0.034)\log(L(\mathrm{H\alpha})) + (-0.684 \pm 1.409), \tag{11}$$

$$\log(L(\mathrm{NUV})) = (0.980 \pm 0.028)\log(L(\mathrm{H\alpha})) + (-0.551 \pm 1.096). \tag{12}$$

Here, Equations (11) and (12) correspond to the correlation of FUV and NUV luminosities with Hα. All luminosities in equations are in $\mathrm{erg\,s^{-1}}$. We also found a correlation for FUV and Hα SFRs for the Balmer decrement and also for JWST 21 μm method, as shown in Figure 5. The linear fit for the

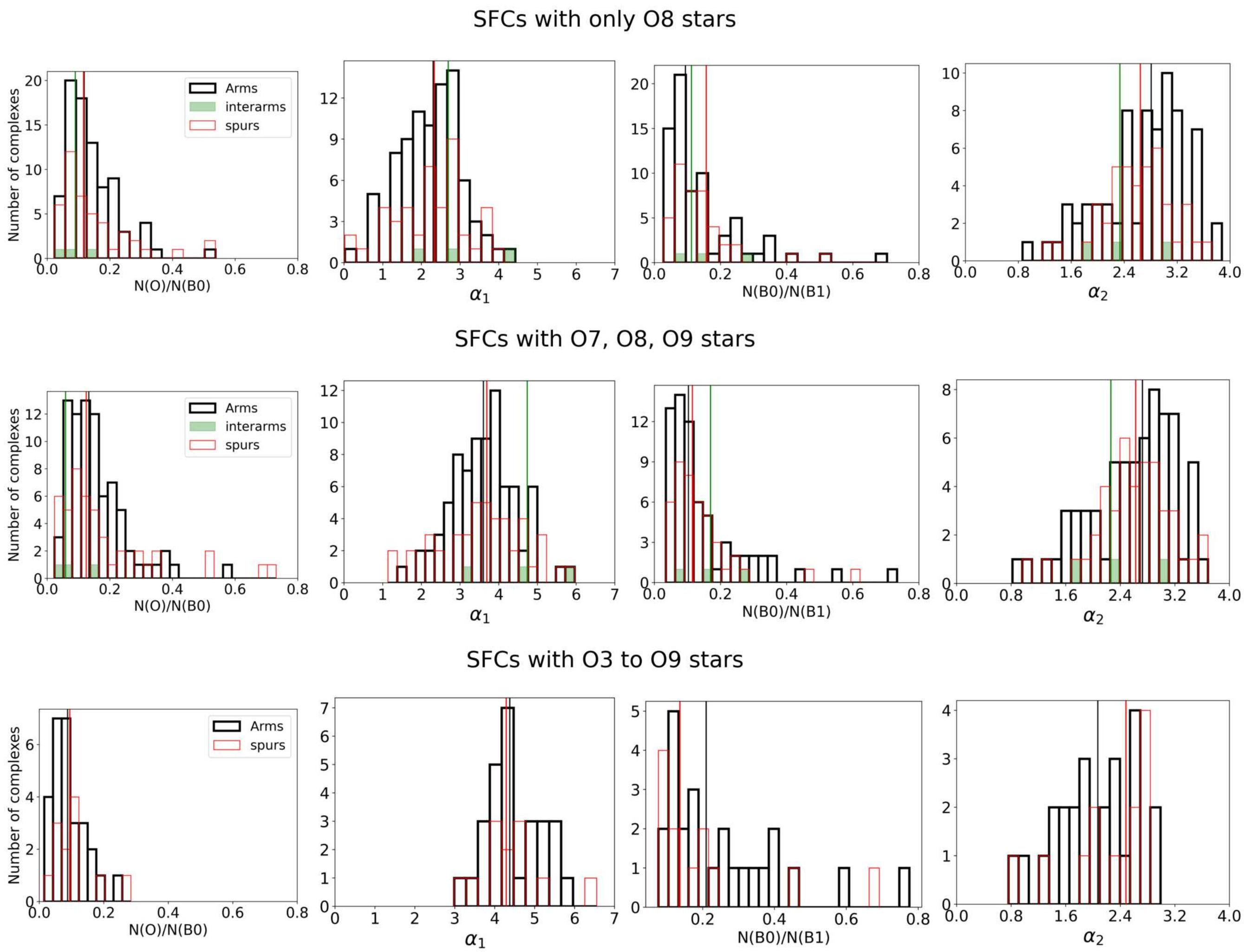

Figure 6. The distribution of $\frac{N(\mathrm{O})}{N(\mathrm{B0})}$, α_1, $\frac{N(\mathrm{B0})}{N(\mathrm{B1})}$ and α_2. The vertical lines represent the median values of the distribution, which are mentioned in Table 2.

Balmer decrement is

$$\log(\mathrm{SFR_{FUV}}) = (0.934 \pm 0.035)\log(\mathrm{SFR_{H\alpha}}) + (-0.455 \pm 0.09) \quad (13)$$

and the linear fit for the JWST 21 μm method is

$$\log(\mathrm{SFR_{FUV}}) = (0.849 \pm 0.043)\log(\mathrm{SFR_{H\alpha}}) + (-1.081 \pm 0.101). \quad (14)$$

From Figure 5, and Equations (13) and (14), we can see that the Hα SFR estimated for Balmer decrement is higher than the JWST method. This again indicates that the different extinction methods correct for extinction at different depths.

We also see that the SFCs in the interarm region do not have higher luminosities than those in the arms and spurs (See Figures 3(c) and (d)). This could happen because interarm SFCs have smaller areas, as seen in Figure 4. The luminosities of SFCs in the arm and spurs span a wide range of values.

The estimated extinction-corrected Hα luminosity of SFCs is between $10^{37} \leqslant L_{\mathrm{H}\alpha} \leqslant 10^{40}$, which is 10 times greater than the values in K. Kreckel et al. (2016). This increase in luminosity could happen because we have convolved the Hα image to a lower resolution, which can cause some clusters to blend into larger ones and potentially increase the contribution of DIGs.

4.3. Determing the IMF of the SFCs

We estimate $\frac{N(\mathrm{O})}{N(\mathrm{B0})}$ and $\frac{N(\mathrm{B0})}{N(\mathrm{B1})}$ and their respective IMF indices α_1 and α_2 in Section 3.4. The distribution of the stellar ratios and IMF indices for the three choices of O-type stars is shown in Figure 6, and the median ratios and IMF index for all the cases are given in Table 2. We used the bootstrapping method to determine the standard error associated with the median ratios and median IMF indices.

When we consider that Hα arises from only the O8V stars, we find that $\alpha_1 = 2.32$ for the arms and spurs, which is closer to the canonical stellar IMF ($\alpha = 2.3$) (P. Kroupa et al. 2024). But when we populate with more types of O stars, such as O7V, O8V, and O9V, and calculate the median ratio for each SFC, we find that the median α_1 becomes steeper ($\alpha_1 = 3.66$) than the canonical IMF, and for the arms and spurs it is again nearly the same. We also noticed that only 2% of SFCs decreased when populated with three types of O stars (O7V, O8V, and O9V), But when we considered the range of O stars (O3V to O9V), we observed a significant decrease in the number of SFCs (69%). In addition, the number of SFCs reduced to 34% in the arms and 27% in the spurs, giving the slope a much steeper value of ($\alpha_1 = 4.35$), with no contribution from interarm SFCs. The decrease in the number of SFCs

Table 2
IMF Parameters in Different Regions

O star Type	Region	No of SFCs	Median $\frac{N(\mathrm{O})}{N(\mathrm{B0})}$	Median α_1	No of SFCs	Median $\frac{N(\mathrm{B0})}{N(\mathrm{B1})}$	Median (α_2)
O8	Arm	84	0.12 ± 0.01	2.30 ± 0.12	71	0.09 ± 0.01	2.81 ± 0.09
	Spurs	44	0.12 ± 0.01	2.33 ± 0.18	42	0.11 ± 0.01	2.64 ± 0.10
	Interarm	3	0.09 ± 0.04	2.69 ± 0.88	3	0.16 ± 0.07	2.34 ± 0.44
(Weighted Mean Value)	⋯	⋯	0.12 ± 0.00	2.32 ± 0.06	⋯	0.10 ± 0.01	2.74 ± 0.10
O7, O8, O9	Arm	80	0.13 ± 0.01	3.60 ± 0.12	67	0.10 ± 0.01	2.72 ± 0.10
	Spurs	44	0.12 ± 0.02	3.69 ± 0.19	42	0.12 ± 0.01	2.62 ± 0.10
	Interarm	3	0.06 ± 0.05	4.73 ± 0.94	3	0.17 ± 0.08	2.26 ± 0.44
(Weighted Mean Value)	⋯	⋯	0.12 ± 0.01	3.66 ± 0.18	⋯	0.11 ± 0.01	2.67 ± 0.08
O3 to O9	Arm	28	0.09 ± 0.01	4.38 ± 0.19	24	0.21 ± 0.04	2.07 ± 0.20
	Spurs	12	0.09 ± 0.02	4.29 ± 0.24	12	0.14 ± 0.05	2.48 ± 0.27
	Interarm	0	⋯	⋯	0	⋯	⋯
(Weighted Mean Value)	⋯	⋯	0.09 ± 0.00	4.35 ± 0.05	⋯	0.19 ± 0.04	2.21 ± 0.21

Note. The weighted mean α_1 and α_2 for all three cases combined is 3.16 ± 0.62 and 2.64 ± 0.14, respectively.

happens because not all SFCs have luminosities large enough to accommodate the different types of massive stars.

However, in contrast to α_1, we find that $\frac{N(\mathrm{B0})}{N(\mathrm{B1})}$ and α_2 do not vary much with different populations of O-type stars. The variation in α_2 is significantly less for the first two cases. But, we see that α_2 is steeper for the arms compared to the interarm SFCs, which is contradictory to what is expected. However, this result is statistically insignificant because we have only three SFCs for the first two cases, and the error is also very high for interarm SFCs. When we populate SFCs with O3V to O9V stars, we find that the SFCs in the arms have IMF slopes that are flatter than the spurs. The arms show a more significant variation in α_2 for the third case compared to the first two cases (which can be up to 0.74). But variation in α_2 is lesser for spurs (up to 0.16). Nonetheless, the reduced variation and smaller uncertainties associated with it make α_2 a more reliable indicator of the IMF index. We have discussed more on this topic in Section 5.

4.4. IMF Trends with the Properties of the SFCs

We plotted the variation of our calculated IMF indices (α_1 and α_2) with the properties of the SFCs as shown in Figure 7. For the first case (SFCs with only O8 stars), the correlation of with α_1 with SFC properties such as FUV − NUV color, $\log_{10}(\Sigma(M_*))$, $\log_{10}(\Sigma(M_{\mathrm{H_2}}))$, and $\log_{10}(\Sigma(\mathrm{SFR}))$ are given by the Spearman correlation coefficients of −0.2, −0.1, −0.1, and −0.3, respectively, which are weak negative correlations. Only with $\log_{10}(\Sigma(\mathrm{SFR}))$ does α_1 show a slightly better correlation. We observed that for the second case (SFCs with O9, O8, and O7 stars), the $\log_{10}(\Sigma(\mathrm{SFR}))$ correlation with α_1 became stronger with the correlation coefficient −0.5, which indicates that as the SFR increases, the IMF becomes flatter, i.e., the number of massive stars increases. The other three properties show similar correlations with α_1 for the second case as for the first one.

In contrast, α_2 shows strong correlations with the properties of the SFCs, the most prominent being the correlation with FUV − NUV color. It has a high Spearman correlation coefficient value of nearly +1 for all the cases. We fitted a quadratic equation to it, as shown below (Equation (15)), and the fitting parameters are given in Table 3 for the different cases,

$$\alpha_2 = a(\mathrm{FUV} - \mathrm{NUV})^2 + b(\mathrm{FUV} - \mathrm{NUV}) + c. \tag{15}$$

The correlation coefficients of $\Sigma(\mathrm{SFR})$ with α_2 are found to be −0.5 and −0.4 for the first two cases. We also fitted a linear regression for the α_2 and $\Sigma(\mathrm{SFR})$ correlations. The equation is given by,

$$\alpha_2 = d \times \log_{10}(\Sigma(\mathrm{SFR})) + e, \tag{16}$$

where the fitting parameters d and e are given in Table 3.

Since the canonical IMF is considered a universal probability density distribution function (T. Jeřábková et al. 2018), we found the corresponding parameters of the SFCs associated with this IMF index so that we can compare it with our estimated IMF. We determined the color and $\log_{10}(\Sigma(\mathrm{SFR}))$ for the canonical stellar IMF value ($\alpha = 2.3$) from Equations (15) and (16) along with Table 3 for all three cases. The color, FUV − NUV ≈ −0.04, and $\log_{10}(\Sigma(\mathrm{SFR})/M_\odot\ \mathrm{yr}^{-1}\ \mathrm{kpc}^{-2}) \approx -1.16$ were estimated for the canonical IMF value. The values are similar for all three cases. Since our median IMF indices are steeper than the canonical values for arms and spurs, we obtain FUV − NUV > − 0.04 and $\log_{10}(\Sigma(\mathrm{SFR})/M_\odot\ \mathrm{yr}^{-1}\ \mathrm{kpc}^{-2}) < -1.16$ for our values.

Apart from FUV−NUV and $\log_{10}(\Sigma(\mathrm{SFR}))$, the $\log_{10}(\Sigma(M_{\mathrm{H_2}}))$ also has a weak negative correlation with α_2, with a correlation coefficient of −0.4. However, this is stronger than the correlation with α_1. Hence, as $\Sigma(M_{\mathrm{H_2}})$ increases α decreases i.e., the IMF becomes flatter. This indicates that the larger the molecular surface mass density in the galaxy disk, the larger are the fraction of high-mass stars. We also see that this correlation generally holds for dense molecular clouds of mass density $\geqslant 10^8 M_\odot \mathrm{kpc}^{-2}$. For less dense clouds, α nearly becomes constant. In Figure 7, in α_2 and $\Sigma(M_{\mathrm{H_2}})$ correlation, there is a fairly sharp cutoff at $\log_{10}(\Sigma(M_{\mathrm{H_2}})/M_\odot\ \mathrm{kpc}^{-2}) = 9.5$ for the third case. But when it comes to $\Sigma(M_*)$, we observed the increase in α_2 with

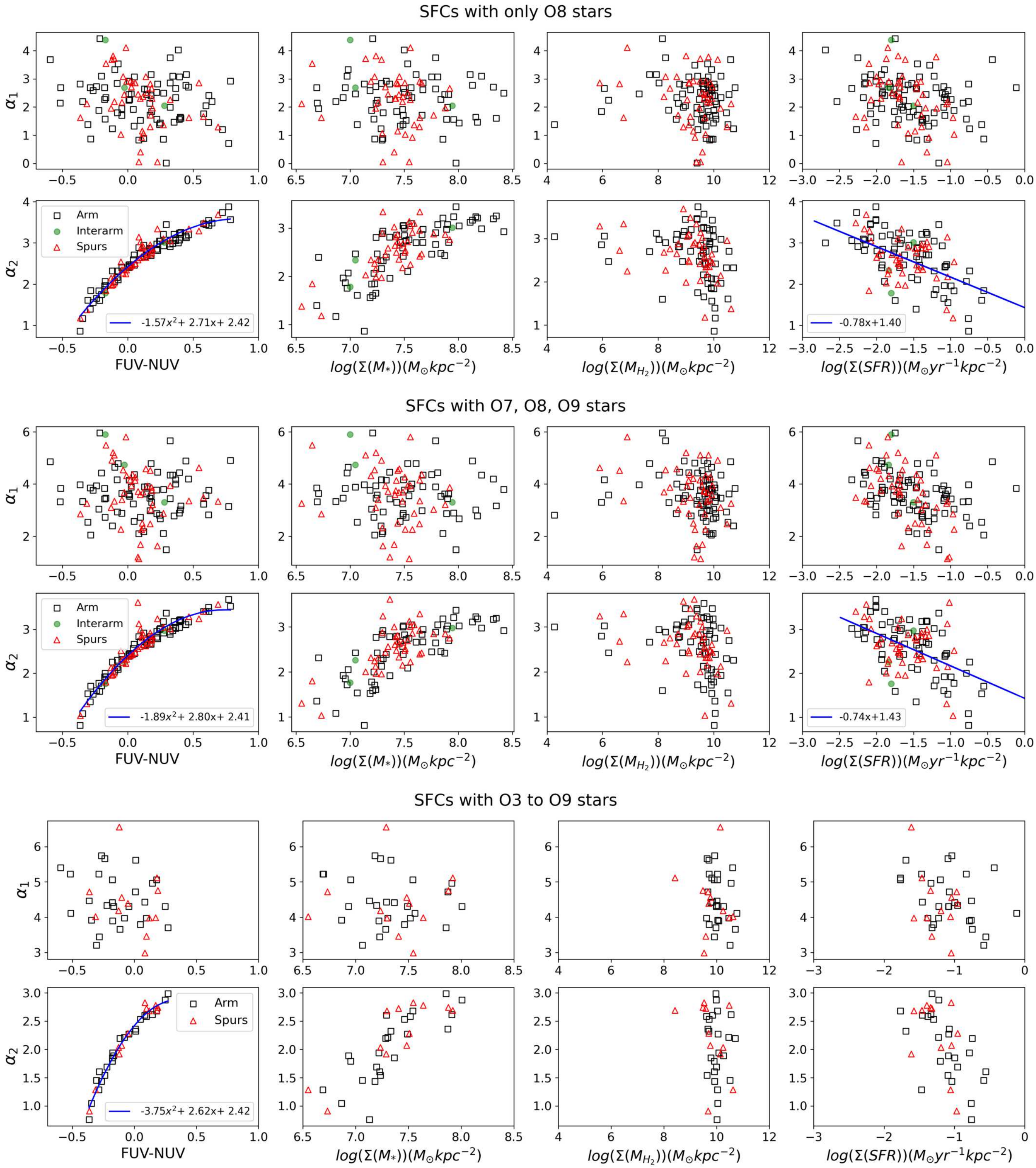

Figure 7. Variation of IMF index (α_1 and α_2) with the different properties of IMF, such as FUV and NUV color, stellar mass density, molecular mass density, and SFR density (from left).

increasing $\Sigma(M_*)$, which means that the IMF becomes steeper as stellar mass density increases, which is contrary to $\Sigma(M_{\mathrm{H}_2})$. This may indicate that the more massive SFCs (i.e., larger $\Sigma(M_*)$) have evolved stellar populations and the massive stars have evolved away. We discuss the significance of these trends in Section 5.

5. Discussion

Our study assumes that the Hα emission mainly arises from O-type stars. But, since we have no information on what kind of O stars populate each SFC, we populated the SFCs with the following combinations: (i) O8V star (whose luminosity

Table 3
Fitting Parameters for α_2 and FUV − NUV Plot (Equation (15)) and α_2 and $\log_{10}(\Sigma(\mathrm{SFR}))$ Plot (Equation (16))

O star Type	*a*	b	*c*	d ($M_\odot^{-1}$ yr kpc^2)	*e*
O8	−1.57 ± 0.15	2.71 ± 0.07	2.42 ± 0.02	−0.78 ± 0.11	1.40 ± 0.18
O7, O8, O9	−1.89 ± 0.18	2.80 ± 0.08	2.41 ± 0.02	−0.74 ± 0.12	1.43 ± 0.19
O3 to O9	−3.75 ± 0.52	2.62 ± 0.11	2.42 ± 0.02	⋯	⋯

Note. *a*, *b*, and *c* are fitting parameters for α_2 and FUV − NUV plot. Whereas, *d* and *e* are fitting parameters for α_2 and $\log_{10}(\Sigma(\mathrm{SFR}))$ plot. The first row or only O8 stars gives the best fit for the α_2 and (FUV − NUV) relation.

corresponds to the median luminosity of the SFCs in NGC 628; (ii) a combination of O7V, O8V, and O9V stars; and (iii) a combination of OV stars with a mass limit of 100 $M_\odot$ (O3V to O9V stars). Then, we generated different possible stellar ratios $\frac{N(\mathrm{O})}{N(\mathrm{B0})}$ and $\frac{N(\mathrm{B0})}{N(\mathrm{B1})}$ for each SFC and noted the median values for each SFC. Hence, there is a range of possibilities for the high-mass IMF, which depends on how we populate O stars in the SFCs. Apart from O stars, there can also be some contribution from very massive B stars in Hα, and we are aware of the degeneracy present in considering the type of the population. But for this study, we will go with the above assumption to see if we can get some estimate of IMF. Even if we consider the contribution from B stars in Hα emission, we might see a variation in the result for option (iii), where we consider populating with all types of O stars.

When we populated the SFCs with different types of O stars, we ensured that all types were present in each SFC. But in reality, this may not be the case. However, it does help us to understand how steep the IMF can go. Studies show that massive O-type stars of mass more than 100 $M_\odot$ are detected in nearby galaxies (V. M. Kalari et al. 2022). J. Koda et al. (2012) have shown that, statistically, for the cluster to have a star as massive as 100 $M_\odot$, it should have a cluster of mass at least $10^5 M_\odot$.

But stochastically, massive stars can form in less massive clusters; alternatively, massive stars might not form in massive clusters. With high stellar density, the inner disk may host clusters with one or more massive stars. In addition, it must be noted that although we see in Figure 4 that the SFC stellar masses are above $10^5 M_\odot$, the SFCs may be hosting multiple clusters that cannot be individually resolved. However, low-mass O stars are more likely to form rather than high-mass stars. We also find that the number of SFCs decreases when we try to populate with higher masses of O stars. So, we conclude that the existence of SFCs with very massive O-type stars in NGC 628 is less probable than the existence of low-mass O-type stars such as O9 to O7 stars.

When considering fully populated SFCs (option (iii)), the IMF becomes top-heavy (i.e., $\alpha > 2.3$, so a steeper IMF) compared to only for O8V stars (option (i)), which is nearly canonical. Hence, the IMF index is steeper than the canonical value at the high-mass end of stellar populations (O stars and massive B stars). But we know that the more massive the stars are, the shorter is their lifetime. Hence, many massive stars must have already passed their main sequence, which could be why the present-day IMF that we observe in NGC 628 appears to be a top-light IMF.

We have derived two IMF indices, α_1 and α_2. Since α_1 is derived from O-type stars that have short lifetimes ($<10^7$yr), it represents the present-day IMF index. On the other hand, α_2 is more dependent on the B-type stars, which have longer lifetimes ($\leqslant 10^8$yr), and hence represent the general high-mass IMF index. However, some emissions from NUV might come from the evolved stellar populations. But as the contribution from main sequence stars will be higher, and since we are taking the SFCs that have emission in other bands too, we can say that the SFCs we have considered have massive stars in them. The α_1 values in Table 2 show a significant variation for different populations of O stars (cases (i), (ii), and (iii)). In contrast, the ratio of high-mass to low-mass B stars, i.e., $N(\mathrm{B0})/N(\mathrm{B1})$, gives a consistent value for all the scenarios. This shows that $\frac{N(\mathrm{B0})}{N(\mathrm{B1})}$ does not depend strongly on what kind of O stars are present in the SFCs. This suggests that the average of α_2 could be a better indicator of the high-mass stellar IMF than the present-day IMF index α_1. The mean value for the IMF index we obtain is $\alpha_2 = 2.64 \pm 0.14$, which is a steeper or top-light IMF compared to the canonical IMF.

Various studies have obtained a top-light IMF compared to the canonical IMF for the massive stars (P. Kroupa 2002). G. E. Miller & J. M. Scalo (1979) and R. C. J. Kennicutt (1983) predicted $\alpha = 2.5$ for masses above $1 M_\odot$. J. M. Scalo (1986b) predicted α is between 2.3 and 3.3 for the high-mass end. Apart from these, D. R. Weisz et al. (2015) found $\alpha = 2.45$ for 85 clusters in M31 and T. M. Wainer et al. (2024) found $\alpha = 2.5$ for the 34 clusters in M33. These studies used the resolved population in clusters to find the high-mass IMF. Most of these studies have the low-mass cutoff for the high-mass IMF as $1 M_\odot$. In our study, there is an overlap in the mass for both $\frac{N(\mathrm{O})}{N(\mathrm{B0})}$ and $\frac{N(\mathrm{B0})}{N(\mathrm{B1})}$ ratios, and we see that both α_1 and α_2 have an average value within the range predicted in J. M. Scalo (1986b).

Studying the stellar IMF in external galaxies is crucial because it allows us to investigate the universality of the IMF within the galaxy as well. R. S. Klessen et al. (2007) showed that the IMF in the star-forming regions of the Milky Way's bulge differs from the IMF in the disk. Multiple studies utilize the complete field of the galaxy and try to understand if there is any IMF variation in the XUV disk of the galaxy compared to the inner disk (J. Koda et al. 2012; S. M. Bruzzese et al. 2019). This is because the IMF can depend on galaxy properties such as stellar densities, gas densities, and metallicity.

The MUSE observations of NGC 628 cover only the inner region. Hence, we try to understand the properties of SFCs in the arm, interarm, and spurs, which are expected to have different environments and star-forming conditions. Unfortunately, only three interarm SFCs have FUV, NUV, and the Hα emission, which is necessary to obtain the IMF index. Hence, the IMF index values we estimated for the interarm region in this study are statistically insignificant. However, as discussed below, our results agree with those of the previous studies.

Table 4
IMF Parameters in Different Regions for SFCs with FUV − NUV ⩽ 0.3

O star Type	Region	No of SFCs	Median $\frac{N(\mathrm{O})}{N(\mathrm{B0})}$	Median α_1	No of SFCs	Median $\frac{N(\mathrm{B0})}{N(\mathrm{B1})}$	Median (α_2)
	Arm	51	0.12 ± 0.01	2.27 ± 0.15	48	0.14 ± 0.02	2.47 ± 0.10
O8	Spurs	37	0.11 ± 0.02	2.36 ± 0.18	37	0.12 ± 0.01	2.54 ± 0.09
	Interarm	3	0.09 ± 0.04	2.69 ± 0.88	3	0.16 ± 0.08	2.34 ± 0.44
(Weighted Mean Value)	…	…	0.12 ± 0.01	2.32 ± 0.08	…	0.13 ± 0.01	2.49 ± 0.04
	Arm	51	0.14 ± 0.01	3.55 ± 0.13	48	0.14 ± 0.02	2.43 ± 0.11
O7, O8, O9	Spurs	37	0.12 ± 0.02	3.68 ± 0.22	37	0.12 ± 0.01	2.54 ± 0.09
	Interarm	3	0.06 ± 0.05	4.73 ± 0.94	3	0.17 ± 0.08	2.26 ± 0.44
(Weighted Mean Value)	…	…	0.13 ± 0.02	3.64 ± 0.20	…	0.13 ± 0.01	2.47 ± 0.06
	Arm	27	0.09 ± 0.01	4.33 ± 0.18	24	0.21 ± 0.04	2.07 ± 0.20
O3 to O9	Spurs	12	0.09 ± 0.02	4.29 ± 0.24	12	0.14 ± 0.05	2.48 ± 0.27
	Interarm	0	…	…	0	…	…
(Weighted Mean Value)	…	…	0.09 ± 0.00	4.32 ± 0.05	…	0.19 ± 0.04	2.21 ± 0.21

Note. The weighted mean α_1 and α_2 for all three cases combined is 3.22 ± 0.6 and 2.43 ± 0.06, respectively.

The SFCs in the interarm regions have smaller areas and mass densities compared to the arms and spurs. Hence, it is expected that the IMF in the interarms will not have enough cluster mass to have more massive stars, making it top-light IMF (P. Kroupa et al. 2024). However, several studies, including K. Kreckel et al. (2016), have shown that there is little difference in star formation properties between arm and interarm SFCs. Our studies show that the IMF value for the interarm region is steeper than the arm and spur regions for $\frac{N(\mathrm{O})}{N(\mathrm{B0})}$, and for $\frac{N(\mathrm{B0})}{N(\mathrm{B1})}$, it is flatter. However, fewer SFCs in the interarm regions make the error bars prominent. J. M. Scalo (1986b) showed that the variation in the IMF with region to region is smaller than ±0.5. Here, the variation of IMF index α_1 in interarm compared to arm and spurs is less than 0.5 for case one, but it becomes more significant for case two. Apart from the three SFCs in the interarm for which we found the high-mass stars ratio, there are more SFCs with only Hα and only NUV emission and no counterparts in the two wavelengths. This shows that there could be stars in the very early stage surrounded by gas and dust, causing extinction in lower wavelengths, and the presence of only NUV in some SFCs indicates that there are even older populations in this region.

There is no statistically significant difference between α_1 in the spurs and the arms for any three cases. The present-day IMF α_1 of the SFCs in the spurs is slightly steeper than the IMF in the arms. The variation is between 0.03 and 0.09. It becomes flatter for α_2, making the arms top light compared to the spurs and interarms. The spurs have nearly the same IMF index for the third case as the first two, but the arms become much flatter, making it top heavy, contrary to what we see for α_1. So α_1 might be the right indicator to check for the universality and compare the nature of high-mass IMF across the region. Meanwhile, how steep or flat α_2 can get might depend on how we populate the O stars, though variation in values for different cases is lesser in α_2.

The variation of high-mass IMF indices with the properties of SFCs, such as SFR, metallicity, and mass of the clusters or galaxies, helps us understand the massive star formation in different environments. The (Σ(SFR)) variation with the IMF is commonly discussed (M. L. P. Gunawardhana et al. 2011; T. Jeřábková et al. 2018; P. Kroupa et al. 2024). Studies have shown that the higher the galaxy or cluster SFR, the more likely it will form high-mass stars because they will have enough mass to produce them (R. B. Larson 2006; M. L. P. Gunawardhana et al. 2011). We see that our SFCs also follow a similar trend. Even α_1, which does not show much trend with any other properties, shows the trend with $\log_{10}(\Sigma(\mathrm{SFR}))$. We fitted a linear regression to the α_2 and $\log_{10}(\Sigma(\mathrm{SFR}))$, and found the relation as in Equation (16) with the parameters mentioned in Table 3. M. L. P. Gunawardhana et al. (2011) also fitted a linear fit for α and $\log_{10}(\Sigma(\mathrm{SFR}))$ for galaxies, which is

$$\alpha = -0.3 \times \log_{10}(\Sigma(\mathrm{SFR})) + 1.7, \tag{17}$$

where α is the IMF index as mentioned in the introduction (Section 1). We find that this relation gives $\log_{10}(\Sigma(\mathrm{SFR}))$ because the α corresponding to the canonical IMF is equal to $-2 M_\odot\ \mathrm{yr}^{-1}\ \mathrm{kpc}^{-2}$, which is lower than what we obtain for our SFCs for high-mass α. This implies that the $\log_{10}(\Sigma(\mathrm{SFR}))$ for the SFCs to produce the canonical IMF is greater than what we see for galaxies. The $\log_{10}(\Sigma(\mathrm{SFR})/M_\odot\ \mathrm{yr}^{-1}\ \mathrm{kpc}^{-2})$ of the inner regions of the Milky Way varies between 0 and -3 (D. Elia et al. 2022). The $\log_{10}(\Sigma(\mathrm{SFR})/M_\odot\ \mathrm{yr}^{-1}\ \mathrm{kpc}^{-2})$, corresponding to canonical IMF found using relation from M. L. P. Gunawardhana et al. (2011), and even our values fall within this range. However, in this study, we estimate for SFCs and not for the whole galaxy.

We find a strong correlation between α_2 and the extinction-corrected UV color, FUV − NUV. We see in our distribution in Figure 4 that the SFCs have a wide range of colors from −0.6 to 0.8. The median color for the SFC distribution in the arms is 0.14, and 0.08 in spurs. J. Koda et al. (2012) discussed that if a cluster has FUV − NUV < 0.2–0.3, i.e., is blue in color, it must contain O and/or B stars. However, it is difficult to differentiate clusters with and without O stars just by looking at the *UV* colors. Even SFCs with FUV − NUV > 0.3 might have O and B stars. Hence, we took blue SFCs with FUV − NUV ⩽ 0.3. We found the median O to B0 and B0 to B1 stellar ratios, along with median α_1 and α_2 values as seen in Table 4. We found that it significantly affects the arm SFC numbers. For the first two cases, the number of SFCs are the same. We also found that taking only blue SFCs does not affect α_1 much. However, α_2 values became less steep, making α_2 closer to the canonical value. For the first two cases, the arms and spurs have nearly the same α_2 values. We also find that spurs become steeper than arms for α_2. We found that the IMF index and FUV−NUV correlations are strong only for α_2. One of the reasons for this could be because we obtain the number of B stars from the FUV and NUV emissions.

The color FUV − NUV > 0 implies that the NUV emission is more than the FUV, i.e., there are fewer massive stars. NUV also comes from some evolved stars that can contribute and make SFCs redder. This can also be seen in the trend. The IMF gets steeper as the SFCs become redder, again showing the bottom heaviness. And for the cases, it starts getting bottom heavy at FUV − NUV > −0.04. Hence, color can also indicate the nature of the IMF.

From our results, we also find that the weak correlation of α_2 with $\Sigma(M_{\mathrm{H_2}})$ is as expected, i.e., as molecular hydrogen mass density increases, the IMF index increases. The more massive and dense the clouds, the higher the probability of forming high-mass stars. The reason for the scatter in the correlation could be that a single conversion factor was considered to obtain the molecular hydrogen mass for all the SFCs. It also seems like the less dense clouds cannot fully populate the O stars. In Figure 7, for case three, molecular clouds barely form massive O stars for $\log(\Sigma(M_{\mathrm{H_2}})/M_{\odot}\mathrm{kpc}^{-2}) < 9.5$ and none below $\log(\Sigma(M_{\mathrm{H_2}})/M_{\odot}\mathrm{kpc}^{-2}) = 8.5$. We also see that most of the data points in all three runs are still clumped between $\alpha_2 = 2$ to 3, as expected from canonical or Salpeter, and some region-to-region variation. The tail to α_1 only appears at the highest $\Sigma(M_{\mathrm{H_2}})$ measured. This shows the importance of molecular cloud surface density in forming massive stars.

The correlation of α_2 with $\Sigma(M_*)$ in our plot seems contradictory to the previous studies. As the SFC $\Sigma(M_*)$ increases, the IMF steepens, implying fewer massive stars are produced. However, we estimated SFC masses from the starburst99 model, and the redder the SFCs, the more massive the complexes are, i.e., they are composed of cooler and older stars. But this does not mean that there were no massive stars before. As said before, the more massive the stars are, the shorter their time in the main sequence will be. Even if these SFCs had very massive stars, they might already be exhausted. Hence, this trend is quite understandable. However, a more accurate estimation of stellar mass might help us understand it better.

We find very few FUV excess young SFCs with low stellar mass that show top-heavy IMF (see α_2 correlation with FUV − NUV in Figure 7.) There are very few in arms and spurs. Some even show nearly Salpeter IMF. These SFCs have large Σ(SFR). This could be an indication of recent starbursts in these SFCs.

Apart from these factors, the IMF also depends upon the metallicity and temperature of the molecular clouds. As we look at the inner disk of a massive galaxy, we expect solar metallicity to be a reasonable assumption, and we do not expect it to vary much. Although not knowing the exact population is a major drawback, this study gives an idea of the IMF in galaxies where the $H\alpha$ mainly comes only from O stars. This result is specific to the galaxy NGC 628, which is a massive grand design spiral galaxy. In future studies, we will apply the same method to explore the IMF in galaxies in different environments and check its universality.

6. Conclusions

In this project, we used Hα from MUSE and FUV and NUV emission from UVIT to determine the IMF of the SFCs in the inner disk of the galaxy NGC 628 by estimating the approximate number of O stars and B stars from each SFC. We also derived some important trends of the IMF index with the properties of the SFCs. The main results of this study are summarized below:

1. There is less FUV emission in the inner disk of NGC 628 compared to Hα and NUV emission, indicating strong extinction and/or more dust-embedded star formation, mainly in the interarm regions.
2. We see a strong correlation between the extinction-corrected UV and Hα luminosities for the Balmer decrement method and 21 μm JWST correction compared to the extinction correction done by the Beta slope method.
3. The properties of SFCs in the arm, spurs, and interarms do not vary much and are consistent with previous studies. However, the area of the SFCs in the interarms is smaller compared to the distribution of SFC areas in arms and spurs.
4. The present-day IMF index α_1 corresponding to $\frac{N(\mathrm{O})}{N(\mathrm{B0})}$ stellar ratio becomes steeper ($\alpha_1 = 4.35 \pm 0.05$) as we populate the SFCs with O-type stars up to stellar masses of 100 $M_{\odot}$ (option 3, Table 2), which is much steeper than the values found in the previous studies. The mean α_1 is around 3.16 ± 0.52. However, the general high-mass IMF index α_2 corresponding to the $\frac{N(\mathrm{B0})}{N(\mathrm{B1})}$ ratio has mean slope of $\alpha_2 = 2.64 \pm 0.14$. The α_2 values are consistent for different O-type stellar populations. However, α_1 for the case where SFCs were populated with only O8 stars has a mean value closer to the canonical stellar IMF.
5. The present-day IMF index α_1 from massive stars ($M > 10M_{\odot}$) is steeper than high-mass IMF index α_2, which we estimated from stars of mass, $10M_{\odot} \geqslant M \geqslant 3M_{\odot}$. This is because the more massive the star is, the lesser is its lifetime in the main sequence.
6. The IMF index in the arms and spurs are similar, showing a variation $<\pm 0.2$. The IMF index α_1 is steeper for the interarm than the IMF index for the arm and spurs. Whereas α_2 gets steeper for the arm than spurs and interarm.
7. The extinction-corrected UV color (FUV−NUV) strongly correlates with α_2. But for FUV−NUV > −0.04, the IMF becomes steeper. Hence, the UV color can also indicate the nature of the IMF.
8. The median value of α_1, when considered SFCs with FUV − NUV $\leqslant$ 0.3 is consistent with the value when considered all the SFCs. But the median value of α_2 becomes less steep with median value $\alpha_2 = 2.43 \pm 0.06$.
9. The $\log_{10}(\Sigma(\mathrm{SFR}))$ versus α_2 shows a similar trend as previous studies for galaxies. But the value $\log_{10}(\Sigma(\mathrm{SFR}))$ for galaxies corresponding to the Salpeter IMF is smaller than what we see for SFCs.
10. In our study, α_2 shows a cutoff at $M_{\mathrm{H_2}} \sim 10^{9.5} M_{\odot}$. On closer inspection, α_2 increases with the increase in the density of molecular gas with a weak correlation, suggesting that low-density clouds cannot support high-mass stars, and most of the SFCs clump around the canonical IMF value.

11. The α_2 and $\Sigma(M_*)$ trend shows that massive and old SFCs must have gone through episodes of star formation. Hence, some high-mass stars must already be in the main sequence turn-off.

12. Young SFCs (FUV − NUV < −0.04) with less stellar mass densities show the top-heavy IMF. They also show the high $\log_{10}(\Sigma(\mathrm{SFR}))$, which suggests the starburst in these SFCs.

Acknowledgments

We thank the referee for their valuable comments. M.D. acknowledges the support of the Science and Engineering Research Board (SERB) Core Research Grant CRG/2022/004531 and the Department of Science and Technology (DST) grant DST/WIDUSHI-A/PM/2023/25(G) for this research. We thank Dr. Kathryn Kreckel for her guidance on using MUSE data. This publication uses the data from the UVIT, which is part of the AstroSat mission of the Indian Space Research Organization (ISRO), archived at the Indian Space Science Data Centre (ISSDC). We gratefully thank all the members of various teams for supporting the project from the early stages of design to launch and observations in orbit.

This work is based on observations made with the NASA/ESA/CSA JWST. The data were obtained from the Mikulski Archive for Space Telescopes at the Space Telescope Science Institute, which is operated by the Association of Universities for Research in Astronomy, Inc., under NASA contract NAS 5-03127. The observations are associated with JWST program 2107. The specific JWST observation analyzed can be accessed via DOI:10.17909/52vt-2g08. This work is based on observations collected at the European Southern Observatory under ESO programs 094.C-0623 (PI: Kreckel), 095.C-0473, 098.C-0484 (PI: Blanc), and 1100.B-0651 (PHANGS-MUSE; PI: Schinnerer), as well as 094.B-0321 (MAGNUM; PI: Marconi), 099.B-0242, 0100.B-0116, 098.B-0551 (MAD; PI: Carollo), and 097.B-0640 (TIMER; PI: Gadotti). This paper makes use of the following ALMA data: ADS/JAO. ALMA#2012.1.00650.S. ALMA is a partnership of ESO (representing its member states), NSF (USA), and NINS (Japan), together with NRC (Canada), MOST and ASIAA (Taiwan), and KASI (Republic of Korea), in cooperation with the Republic of Chile. The Joint ALMA Observatory is operated by ESO, AUI/NRAO, and NAOJ. The National Radio Astronomy Observatory is a facility of the National Science Foundation operated under a cooperative agreement by Associated Universities, Inc.

Facilities: Astrosat(UVIT), VLT:Yepun(MUSE), JWST (21μm), ALMA.

Software: Astropy (Astropy Collaboration et al. 2013, 2018), Source Extractor (E. Bertin & S. Arnouts 1996; K. Barbary 2016), Topcat (M. B. Taylor 2005), IRAF (D. Tody 1993), Matplotlib (J. D. Hunter 2007), NumPy (C. R. Harris et al. 2020), Photutils (L. Bradley et al. 2022).

Appendix

We have tabulated the estimated properties of SFCs as Table A1. The entire table for all SFCs is available in machine-readable form.

Table A1
Catalog of Estimated Properties of SFCs

R.A.(J2000) (deg)	Decl.(J2000) (deg)	Filters	Region	Area (arcsec^2)	$A_{H\alpha}$ (mag)	$\Delta A_{H\alpha}$ (mag)	$L_{H\alpha}$ ($10^3 L_\odot$)	$\Delta L_{H\alpha}$ ($10^3 L_\odot$)	L_{FUV} ($10^6 L_\odot$)	ΔL_{FUV} ($10^6 L_\odot$)	L_{NUV} ($10^6 L_\odot$)	ΔL_{NUV} ($10^6 L_\odot$)	$SFR_{H\alpha}$ ($10^{-4} M_\odot$ yr^{-1})	$\Delta SFR_{H\alpha}$ ($10^{-4} M_\odot$ yr^{-1})	SFR_{FUV} ($10^{-3} M_\odot$ yr^{-1})	ΔSFR_{FUV} ($10^{-3} M_\odot$ yr^{-1})	Color (mag)	log(M_{H_2}) ($M_\odot$)	log(M_*) ($M_\odot$)
24.19352898	15.75866545	All	arm	13	1.07	0.01	203.35	0.6	18.9	1.65	2.05	0.13	41.22	0.12	7.19	0.02	−0.52	8.16	5.14
24.18308751	15.79047867	All	arm	15.4	0.43	0.03	19.24	0.31	1.6	0.17	0.27	0.02	3.9	0.065	0.61	0.02	−0.05		5.23
24.14929603	15.79338057	All	arm	9.9	0.88	0.01	63.25	0.34	10.64	0.9	1.54	0.09	12.83	0.07	4.06	0.02	−0.2	7.75	5.3
24.15068082	15.79135657	All	arm	18.8	0.92	0.02	35.81	0.44	16.15	1.2	2.32	0.12	7.25	0.09	6.14	0.02	−0.21	6.76	5.82
24.16830729	15.81789135	All	arm	18.7	1.28	0	559.33	1.2	27.97	2.82	3.76	0.24	113.32	0.241	10.63	0.02	−0.28	8.52	5.84
24.19055832	15.75534162	All	arm	29.2	0.52	0.02	37.11	0.37	4.08	0.31	0.73	0.04	7.55	0.076	1.56	0.02	0.03	7.68	5.85
24.15250999	15.7895322	All	arm	22	1.11	0.01	215.11	0.91	26.11	2.1	3.58	0.19	43.59	0.187	9.93	0.02	−0.27	8.6	5.86
24.16370025	15.79534197	All	arm	70.8	0.73	0.02	258.23	2.69	33.46	1.3	4.47	0.14	52.38	0.548	12.66	0.04	−0.29	9.22	5.87
24.17619665	15.80583753	All	arm	20.9	1.01	0.01	180.08	0.5	23.63	1.68	3.32	0.16	36.51	0.103	8.99	0.02	−0.24	8.3	5.89

Note. Here, R.A.(J2000) and decl.(J2000) are the R.A. and decl. of the SFCs. Filters are wave bands in which SFCs are present. The region represents the SFC's location. Area is the area of the SFCs in arcsec^2. $A_{H\alpha}$ and $\Delta A_{H\alpha}$ is the Hα extinction coefficient and error associated. $L_{H\alpha}$, L_{FUV} and L_{NUV} are the extinction-corrected Hα, FUV and NUV luminosities, respectively. $\Delta L_{H\alpha}$, ΔL_{FUV} and ΔL_{NUV} are the error associated with respective luminosities. $SFR_{H\alpha}$ and $\Delta SFR_{H\alpha}$ are the Hα SFR and respective errors. Similarly, SFR_{FUV} and ΔSFR_{FUV} are the FUV SFR and respective errors. Color is a difference in extinction-corrected FUV and NUV magnitudes. log(M_{H_2}) is molecular hydrogen mass. log(M_*) is the stellar mass of the SFCs.

(This table is available in its entirety in machine-readable form in the online article.)

ORCID iDs

S Amrutha https://orcid.org/0009-0005-6072-9252
Mousumi Das https://orcid.org/0000-0001-8996-6474

References

Adamo, A., Ryon, J. E., Messa, M., et al. 2017, ApJ, 841, 131
Amrutha, S., Das, M., & Yadav, J. 2024, MNRAS, 530, 2199
Anand, G. S., Lee, J. C., Van Dyk, S. D., et al. 2020, MNRAS, 501, 3621
Astropy Collaboration, Price-Whelan, A. M., Sipőcz, B. M., et al. 2018, AJ, 156, 123
Astropy Collaboration, Robitaille, T. P., Tollerud, E. J., et al. 2013, A&A, 558, A33
Barbary, K. 2016, JOSS, 1, 58
Bastian, N., Covey, K. R., & Meyer, M. R. 2010, ARA&A, 48, 339
Bayo, A., Rodrigo, C., Barrado Y Navascués, D., et al. 2008, A&A, 492, 277
Belfiore, F., Leroy, A. K., Williams, T. G., et al. 2023, A&A, 678, A129
Bertin, E., & Arnouts, S. 1996, A&AS, 117, 393
Boselli, A., Boissier, S., Cortese, L., et al. 2009, ApJ, 706, 1527
Bradley, L., Sipőcz, B., Robitaille, T., et al. 2022, astropy/photutils: 1.5.0, v2.2.0, Zenodo, doi:10.5281/zenodo.6825092
Bruzual, G., & Charlot, S. 2003, MNRAS, 344, 1000
Bruzzese, S. M., Thilker, D. A., Meurer, G. R., et al. 2019, MNRAS, 491, 2366
Calzetti, D., Armus, L., Bohlin, R. C., et al. 2000, ApJ, 533, 682
Calzetti, D., Chandar, R., Lee, J. C., et al. 2010, ApJL, 719, L158
Calzetti, D., Kinney, A. L., & Storchi-Bergmann, T. 1994, ApJ, 429, 582
Calzetti, D., Kennicutt, R. C., Engelbracht, C. W., et al. 2007, ApJ, 666, 870
Calzetti, D., Lee, J. C., Sabbi, E., et al. 2015, AJ, 149, 51
Carvalho, A. S., Hillenbrand, L. A., France, K., & Herczeg, G. J. 2024, ApJL, 973, L40
Castelli, F., & Kurucz, R. L. 2004, in IAU Symp. 210, Modelling of Stellar Atmospheres, ed. N. Piskunov, W. W. Weiss, & D. F. Gray (San Francisco, CA: ASP), A20
Chabrier, G. 2003, PASP, 115, 763
Chappell, D., & Scalo, J. 2001, MNRAS, 325, 1
Das, M., Yadav, J., Patra, N., et al. 2021, JApA, 42, 85
de Vaucouleurs, G., de Vaucouleurs, A., Corwin, H. G. J., et al. 1991, Third Reference Catalogue of Bright Galaxies (Berlin: Springer)
Dib, S. 2014, MNRAS, 444, 1957
Eden, D. J., Moore, T. J. T., Morgan, L. K., Thompson, M. A., & Urquhart, J. S. 2013, MNRAS, 431, 1587
Elia, D., Molinari, S., Schisano, E., et al. 2022, ApJ, 941, 162
Elmegreen, D. M., Elmegreen, B. G., Adamo, A., et al. 2014, ApJL, 787, L15
Emsellem, E., Schinnerer, E., Santoro, F., et al. 2022, A&A, 659, A191
Foyle, K., Rix, H.-W., Walter, F., & Leroy, A. K. 2010, ApJ, 725, 534
Freyer, T., Hensler, G., & Yorke, H. W. 2003, ApJ, 594, 888
Garn, T., & Best, P. N. 2010, MNRAS, 409, 421
Gavazzi, G., Bonfanti, C., Sanvito, G., Boselli, A., & Scodeggio, M. 2002, ApJ, 576, 135
Gogarten, S. M., Dalcanton, J. J., Williams, B. F., et al. 2009, ApJ, 691, 115
Gunawardhana, M. L. P., Hopkins, A. M., Sharp, R. G., et al. 2011, MNRAS, 415, 1647
Hao, C.-N., Kennicutt, R. C., Johnson, B. D., et al. 2011, ApJ, 741, 124
Harris, C. R., Millman, K. J., van der Walt, S. J., et al. 2020, Natur, 585, 357
Hoversten, E. A., & Glazebrook, K. 2008, ApJ, 675, 163
Hunter, D. A., Elmegreen, B. G., & Ludka, B. C. 2010, AJ, 139, 447
Hunter, J. D. 2007, CSE, 9, 90
Jeřábková, T., Zonoozi, A. H., Kroupa, P., et al. 2018, A&A, 620, A39
Kalari, V. M., Horch, E. P., Salinas, R., et al. 2022, ApJ, 935, 162
Kennicutt, R. C. J. 1983, ApJ, 272, 54
Kennicutt, R. C. J. 1992, ApJ, 388, 310
Kennicutt, R. C. J., Hao, C.-N., Calzetti, D., et al. 2009, ApJ, 703, 1672
Kim, W.-T., & Ostriker, E. C. 2002, ApJ, 570, 132
Klessen, R. S., Spaans, M., & Jappsen, A.-K. 2007, MNRAS: Letters, 374, L29
Koda, J., Yagi, M., Boissier, S., et al. 2012, ApJ, 749, 20
Kreckel, K., Blanc, G. A., Schinnerer, E., et al. 2016, ApJ, 827, 103
Kreckel, K., Faesi, C., Kruijssen, J. M. D., et al. 2018, ApJL, 863, L21
Kroupa, P. 2001, MNRAS, 322, 231
Kroupa, P. 2002, Sci, 295, 82
Kroupa, P., Gjergo, E., Jerabkova, T., & Yan, Z. 2024, arXiv:2410.07311
Krumholz, M. R. 2014, PhR, 539, 49
Kumar, A., Ghosh, S. K., Hutchings, J., et al. 2012, Proc. SPIE, 8443, 84431N
Lang, P., Meidt, S. E., Rosolowsky, E., et al. 2020, ApJ, 897, 122
Larson, R. B. 2006, RMxAC, 26, 55
Lee, J. C., de Paz, A. G., Tremonti, C., et al. 2009, ApJ, 706, 599
Lee, J. C., Sandstrom, K. M., Leroy, A. K., et al. 2023, ApJL, 944, L17
Leitherer, C., Ortiz Otálvaro, P. A., Bresolin, F., et al. 2010, ApJS, 189, 309
Leitherer, C., Schaerer, D., Goldader, J. D., et al. 1999, ApJS, 123, 3
Leroy, A. K., Hughes, A., Liu, D., et al. 2021a, ApJS, 255, 19
Leroy, A. K., Sandstrom, K. M., Lang, D., et al. 2019, ApJS, 244, 24
Leroy, A. K., Schinnerer, E., Hughes, A., et al. 2021b, ApJS, 257, 43
Leroy, A. K., Walter, F., Brinks, E., et al. 2008, AJ, 136, 2782
Lomaeva, M., De Looze, I., Saintonge, A., & Decleir, M. 2022, MNRAS, 517, 3763
Maraston, C. 2005, MNRAS, 362, 799
Martin, D. C., Fanson, J., Schiminovich, D., et al. 2005, ApJL, 619, L1
Meurer, G. R., Wong, O. I., Kim, J. H., et al. 2009, ApJ, 695, 765
Miller, G. E., & Scalo, J. M. 1979, ApJS, 41, 513
Moustakas, J. R. C., Kennicutt, J., & Tremonti, C. A. 2006, ApJ, 642, 775
Osterbrock, D. E. 1989, Astrophysics of Gaseous Nebulae and Active Galactic Nuclei (Mill Valley, CA: Univ. Science Books)
Pflamm-Altenburg, J., & Kroupa, P. 2008, Natur, 455, 641
Postma, J. E., & Leahy, D. 2017, PASP, 129, 115002
Reddy, N. A., Oesch, P. A., Bouwens, R. J., et al. 2018, ApJ, 853, 56
Ryon, J. E., Bastian, N., Adamo, A., et al. 2015, MNRAS, 452, 525
Salim, S., Rich, R. M., Charlot, S., et al. 2007, ApJS, 173, 267
Salpeter, E. E. 1955, ApJ, 121, 161
Sandstrom, K. M., Leroy, A. K., Walter, F., et al. 2013, ApJ, 777, 5
Scalo, J. 1990, in Windows on Galaxies, ed. G. Fabbiano, J. S. Gallagher, & A. Renzini (Dordrecht: Springer), 125
Scalo, J. M. 1986a, FCPh, 11, 1
Scalo, J. M. 1986b, in IAU Symp. 116, Luminous Stars and Associations in Galaxies, ed. C. W. H. De Loore, A. J. Willis, & P. Laskarides (Dordrecht: D. Reidel), 451
Schlafly, E. F., & Finkbeiner, D. P. 2011, ApJ, 737, 103
Sharda, P., & Krumholz, M. R. 2022, MNRAS, 509, 1959
Shetty, R., & Ostriker, E. C. 2006, ApJ, 647, 997
Stedman, S., & Knapen, J. H. 2001, Ap&SS, 276, 517
Sternberg, A., Hoffmann, T. L., & Pauldrach, A. W. A. 2003, ApJ, 599, 1333
Tandon, S. N., Hutchings, J. B., Ghosh, S. K., et al. 2017, JApA, 38, 28
Tandon, S. N., Postma, J., Joseph, P., et al. 2020, AJ, 159, 158
Tanvir, T. S., Krumholz, M. R., & Federrath, C. 2022, MNRAS, 516, 5712
Taylor, M. B. 2005, in ASP Conf. Ser. 347, Astronomical Data Analysis Software and Systems XIV, ed. P. Shopbell, M. Britton, & R. Ebert (San Francisco, CA: ASP), 29
Thilker, D. A., Bianchi, L., Boissier, S., et al. 2005, ApJL, 619, L79
Thilker, D. A., Bianchi, L., Meurer, G., et al. 2007, ApJS, 173, 538
Tody, D. 1993, in ASP Conf. Ser. 52, Astronomical Data Analysis Software and Systems II, ed. R. J. Hanisch, R. J. V. Brissenden, & J. Barnes (San Francisco, CA: ASP), 173
Ujjwal, K., Kartha, S. S., Subramanian, S., et al. 2022, MNRAS, 516, 2171
Wainer, T. M., Williams, B. F., Johnson, L. C., et al. 2024, AJ, 168, 86
Weidner, C., Kroupa, P., & Pflamm-Altenburg, J. 2011, MNRAS, 412, 979
Weisz, D. R., Johnson, L. C., Foreman-Mackey, D., et al. 2015, ApJ, 806, 198
Yadav, J., Das, M., Patra, N. N., et al. 2021, ApJ, 914, 54
Zaritsky, D., & Christlein, D. 2007, AJ, 134, 135